



# Ghostly Strong Ly $\alpha$ Absorbers: Tracers of Gas Flows in the Close Vicinity of Quasars?

Hassan Fathivavsari

School of Astronomy, Institute for Research in Fundamental Sciences (IPM), P.O. Box 19395-5531, Tehran, Iran; [h.fathie@gmail.com](mailto:h.fathie@gmail.com)

Received 2018 August 20; revised 2019 October 2; accepted 2019 November 19; published 2020 January 10

## Abstract

We have searched the Sloan Digital Sky Survey Data Release 12 for ghostly strong Ly $\alpha$  (DLA) systems. These systems, located at the redshift of the quasars, show strong absorption from low-ionization atomic species but reveal no H I Ly $\alpha$  absorption. Our search has, for the first time, resulted in a sample of 30 homogeneously selected ghostly absorbers with  $z_{\text{QSO}} > 2.0$ . Thirteen of the ghostly absorbers exhibit absorption from other H I Lyman series lines. The lack of Ly $\alpha$  absorption in these absorbers is consistent with them being dense and compact with projected sizes smaller than the broad-line region of the background quasar. Although uncertain, the estimated median H I column density of these absorbers is  $\log N(\text{H I}) \sim 21.0$ . We compare the properties of ghostly absorbers with those of eclipsing DLAs that are high-column-density absorbers, located within  $1500 \text{ km s}^{-1}$  of the quasar emission redshift and showing strong Ly $\alpha$  emission in their DLA trough. We discover an apparent sequence in the observed properties of these DLAs, with ghostly absorbers showing wider H I kinematics, stronger absorptions from high-ionization species, C II and Si II excited states, and a higher level of dust extinction. Since we estimate that all these absorbers have similar metallicities,  $\log Z/Z_{\odot} \sim -1.0$ , we conclude that ghostly absorbers are part of the same population as eclipsing DLAs, except that they are denser and located closer to the central active galactic nuclei.

*Unified Astronomy Thesaurus concepts:* [Interstellar absorption \(831\)](#); [Interstellar line absorption \(843\)](#); [Quasars \(1319\)](#); [Active galactic nuclei \(16\)](#); [Quasar absorption line spectroscopy \(1317\)](#); [Intergalactic medium \(813\)](#); [Interstellar dust extinction \(837\)](#); [Circumgalactic medium \(1879\)](#); [Extragalactic astronomy \(506\)](#); [Galaxy structure \(622\)](#); [Galactic winds \(572\)](#)

*Supporting material:* machine-readable table

## 1. Introduction

The feeding habits of supermassive black holes (SMBHs), residing at the center of distant galaxies, and the subsequent feedback from their active galactic nuclei (AGNs) are among the processes key to understanding how galaxies and their SMBHs coevolve (Audibert et al. 2017; Dutta et al. 2018). Simulations have shown that AGNs are primarily fed by the infall of gas into the gravitational potential well of SMBHs (Martin et al. 2016). The infall of gas occurs preferentially through so-called *cold flows* along the filaments of the cosmic web (Kereš et al. 2005; Rahmani et al. 2018a). Direct, unambiguous detection of cold accretion flows onto galaxies has proven to be extremely challenging (Rauch et al. 2008; Cresci et al. 2010; Steidel et al. 2010; Gialavisco et al. 2011). Instead, AGN- or supernova-driven outflows are commonly observed as blueshifted absorption lines in the spectra of galaxies and quasars (Srianand et al. 2002; Chisholm et al. 2015; Wood et al. 2015; Schroetter et al. 2016; Sur et al. 2016; Finley et al. 2017; Rahmani et al. 2018b).

It is expected that chemically young infalling gas should be detected as redshifted absorption lines in the spectra of galaxies and quasars (Kimm et al. 2011; Stewart et al. 2011a). However, the intrinsically weak absorption produced by the low-metallicity and low-velocity infalling gas, along with the possible contamination of these weak absorption lines with the strong absorption from the interstellar medium of the galaxy or enriched outflowing gas, makes it difficult to confidently detect absorption signals from the cold flows in the spectra of galaxies and quasars (Stewart et al. 2011a, 2011b; Kimm et al. 2011; Rubin et al. 2012). Simulations show that if a cold flow is exactly aligned with the line of sight, then some signal might

be detected. However, in practice, this configuration is highly unlikely as one would need to survey an overwhelmingly large number of quasar and galaxy spectra in order to moderately increase the chances of finding such a configuration along a line of sight (Faucher-Giguère & Kereš 2011; Kimm et al. 2011). Although it is extremely difficult to directly observe infalling gas through spectroscopy, its indirect effects on galaxies could still be more conveniently observed (Goerdt et al. 2010; Fumagalli et al. 2011; Lehner et al. 2012; van de Voort et al. 2012). For example, one important piece of indirect evidence for the presence of the cold flow accretion onto galaxies is the dilution of the gas metallicity by the metal-poor infalling gas in the nuclear regions of galaxies (Rupke et al. 2010; Di Matteo et al. 2011; Torrey et al. 2012; Sillero et al. 2017).

It could be possible that a stream of metal-poor infalling gas, on its way to the inner region of a quasar host galaxy, collides with the enriched AGN- or supernova-driven outflowing gas. Upon collision, the two gases get mixed, shock heated, and compressed to a high density (Namekata et al. 2014). If the density is high enough, then the gas becomes optically thick, and it produces a damped Ly $\alpha$  (DLA) absorption when located along the line of sight to the background quasar or galaxy (van de Voort et al. 2012). Since the resulting DLA and the background quasar have almost similar redshifts, the DLA can act as a natural coronagraph and block the strong Ly $\alpha$  emission from the broad-line region (BLR) of the quasar. This would then allow us, depending on the size of these so-called *eclipsing* DLAs, to detect weaker emission from some star-forming regions in the host galaxy or from the narrow-line region (NLR) of the quasar (Hennawi et al. 2009; Finley et al. 2013;

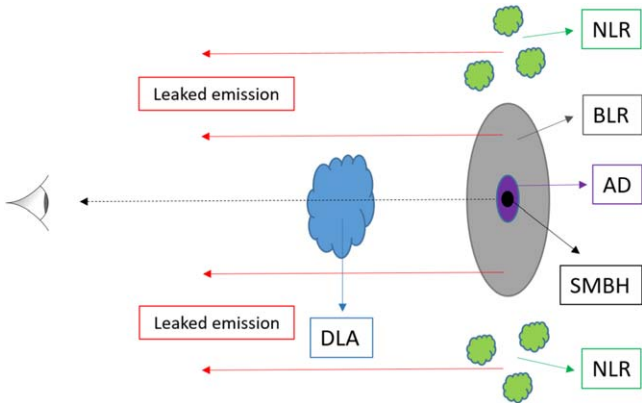


**Figure 1.** Illustration of the DLA–QSO configuration that can lead to the formation of ghostly absorbers in quasar spectra. The continuum from the accretion disk (AD) is fully blocked by the DLA absorber, while only part of the BLR is covered. As a result, the leaked Ly $\alpha$  emission from the regions of the BLR and NLR that are not covered by the cloud would sufficiently elevate the flux level at the bottom of the DLA to form a ghostly absorber.

Fathivavsari et al. 2015, 2016, 2018). The Ly $\alpha$  emission would be detected in the DLA absorption core. If the optically thick H I cloud continuously covers the full extent of the Ly $\alpha$ -emitting region, then no emission is seen in the DLA core.

If an eclipsing DLA cloud is located closer to the quasar, then it would have a higher density and smaller dimensions. Such a small DLA cloud would then cover a smaller fraction of the background Ly $\alpha$ -emitting regions (i.e., star-forming regions or NLR). Accordingly, in the quasar spectrum, one would detect stronger, narrow Ly $\alpha$  emission in the DLA trough. In extreme cases where the density of the gas is very high ( $n_{\text{H I}} > 1000 \text{ cm}^{-3}$ ) and the size of the DLA is smaller than that of the BLR, the leaked emission from the BLR would almost fully fill the DLA absorption trough. In this case, we will have a *ghostly* absorber as no H I absorption is detected in the quasar spectrum (Fathivavsari et al. 2017; Xie et al. 2018). Figure 1 illustrates the DLA–QSO configuration leading to the formation of a ghostly absorber in quasar spectra. As shown in this figure, the continuum from the accretion disk (AD) is fully blocked by the absorber, while only part of the BLR is covered. As a result, the leaked Ly $\alpha$  emission from the regions of the BLR (together with the NLR) that are not covered by the cloud would sufficiently elevate the flux level at the bottom of the Ly $\alpha$  absorption to form a ghostly absorber. Observationally, ghostly absorbers are identified by the presence of strong low-ionization metal absorption lines (e.g., O I, C II, Si II) in the spectra. Since eclipsing DLAs and ghostly absorbers probe regions close to the central engine of the quasar, their characterization is extremely important for understanding the mechanisms by which the gas is accreted onto or ejected by the AGN. Moreover, a detailed study of these systems will also provide important clues for characterizing the spatial structure of the NLR and BLR in AGNs.

In order to study the properties of the eclipsing DLAs and ghostly absorbers, statistically, we recently searched the SDSS-III Baryon Oscillation Spectroscopic Survey Data Release 12 (BOSS; Dawson et al. 2013) for such absorbers. The results on eclipsing DLAs are presented in Fathivavsari et al. (2018). In the current paper, we focus on characterizing the ghostly absorber systems.

## 2. Method

### 2.1. Finding Ghostly Absorbers

Conventional approaches to finding DLAs require absorption with a damping wing to be present in the spectrum or the flux at the bottom of the absorption to be at zero level (Prochaska & Herbert-Fort 2004). However, since the DLA trough in a ghostly absorber is almost fully filled with the leaked emission from the BLR (Fathivavsari et al. 2017), such methods are not well suited for finding these DLAs. We, therefore, use the metal template technique (Herbert-Fort et al. 2006; Fathivavsari et al. 2014) to search for ghostly absorbers in SDSS-BOSS spectra. The metal template technique identifies DLA candidates by cross-correlating the observed spectra with an absorption template made up of several strong metal absorption lines generally detected in DLAs. Detailed descriptions of the technique are presented in Paper I. Below, we briefly explain the outline of the approach.

In our search for ghostly absorbers, we take into account only those quasars that have emission redshift higher than  $z_{\text{em}} = 2.0$ , zero balnicity index (Weymann et al. 1991; Pâris et al. 2017), and continuum-to-noise ratio above 4.0. Employing these criteria on the BOSS spectra leaves us with 149,378 quasars. This sample of quasars is called the  $S_{\text{QSO}}^1$  sample. For each quasar in the  $S_{\text{QSO}}^1$  sample, we cross-correlate its spectrum with the metal absorption template, and then record systems when their correlation function has a maximum with high significance ( $\geq 4\sigma$ ). Similar to eclipsing DLAs, the search for ghostly absorbers is also performed within  $1500 \text{ km s}^{-1}$  of the quasar redshift. Applying this constraint on the  $S_{\text{QSO}}^1$  sample returns 45,040 systems, many of which are false-positive detections. This new sample is called the  $S_{\text{QSO}}^2$  sample.

In order to exclude the spurious systems from the  $S_{\text{QSO}}^2$  sample, we measure the equivalent width (EW) and its corresponding error ( $\sigma_w$ ) for all metal transitions used in the template. We then exclude those systems that have less than three absorption lines detected above  $3\sigma$ . With this constraint, we are left with 10,224 systems. We call this sample the  $S_{\text{QSO}}^3$  sample. In principle, the  $S_{\text{QSO}}^3$  sample comprises Lyman limit systems (LLSs), sub-DLAs (i.e., absorbers with H I column densities,  $\log N(\text{H I}) \leq 20.30$ ), DLAs, ghostly absorbers, and some false-positive detections. Since ghostly absorbers exhibit no DLA absorption, we first exclude from the  $S_{\text{QSO}}^3$  sample those spectra in which a DLA absorption is present. For this purpose, we cross-correlate each observed spectrum in the  $S_{\text{QSO}}^3$  sample with a series of synthetic DLA absorption profiles corresponding to  $N(\text{H I})$  in the range  $19.0 \leq \log N(\text{H I}) \leq 22.50$ . If a DLA absorption is present in the spectrum, the correlation coefficient will be larger than 0.7 and the system is rejected. Employing this algorithm on the  $S_{\text{QSO}}^3$  sample returns 6702 systems. This new sample is called the  $S_{\text{QSO}}^4$  sample. We note that a strong (e.g. C II) metal absorption from some intervening systems (occurring at the expected position of the Ly $\alpha$  absorption from a ghostly absorber) could mimic a Ly $\alpha$  absorption with  $\log N(\text{H I}) < 19.0$ . That is why the synthetic DLA absorptions are constructed for  $\log N(\text{H I}) \geq 19.0$ .

The  $S_{\text{QSO}}^4$  sample contains LLSs with  $\log N(\text{H I}) < 19.0$ , ghostly absorbers, and some false-positive detections. To further exclude the false-positive detections from the  $S_{\text{QSO}}^4$  sample, we cross-correlate each spectrum with an absorption template made up of the Si IV and C IV doublet transitions. It is worth

**Table 1**  
Ghostly Absorbers

SDSS Name	$z_{\text{QSO}}$	$z_{\text{abs}}$	$\log N(\text{H I})$	Fe II(1)	Fe II(2)	Fe II(3)	Al II	Mg II	C II	$f_{\nu}$	$L_{\nu}$
000943.73+132032.6	2.378	2.376	...	892	2722	...	1953	...	3314	1.50	41.7
000958.65+015755.1	2.973	2.976	20.30	39	...	...	278	...	1350	2.70	42.3
001316.82-093841.2	2.636	2.628	21.30	335	...	...	420	...	1027	4.40	42.3
003901.47+073434.2	2.267	2.274	...	...	...	...	1680	3391	2712	1.10	41.6
005343.38+125659.6	2.365	2.371	...	247	...	...	1427	2777	2595	1.00	41.6
011145.03-030138.6	2.275	2.275	...	712	...	2239	...	2362	...	1.90	41.8
022227.99+000523.8	2.882	2.886	21.35	...	...	...	...	...	1127	0.50	41.5
082726.75+214557.0	2.622	2.617	21.30	264	...	...	...	...	...	2.60	42.1
083148.72+020505.9	2.165	2.168	...	413	...	2128	895	3212	1882	1.40	41.6
090424.08+560205.4	2.065	2.072	...	693	...	1110	1594	2685	2937	1.70	41.6
092334.18+102927.7	3.390	3.387	20.30	201	...	...	570	...	2024	2.20	42.3
100448.14+524043.7	2.326	2.316	...	1212	1687	...	1420	3380	2332	0.90	41.5
101422.86+265339.6	2.268	2.264	...	240	1867	2327	1626	3250	2147	0.90	41.5
111649.37+365519.5	2.832	2.834	21.75	...	1207	...	...	...	1834	1.60	42.0
124202.03-002208.9	2.379	2.379	...	192	770	1095	799	...	1565	2.60	42.0
124329.71+014438.8	2.297	2.300	...	...	...	2496	...	2409	2869	1.20	41.6
124847.63+332500.3	2.038	2.035	...	2373	4319	5869	3278	4363	5105	5.80	42.2
125437.96+315530.8	2.299	2.301	...	...	...	816	929	1562	1138	1.40	41.7
130552.24+263300.0	3.046	3.040	21.20	573	2266	...	1275	...	2703	1.10	41.9
134103.38+490735.6	2.290	2.290	...	687	1933	2505	1571	3730	2835	2.40	41.9
134659.96+373454.1	2.619	2.612	21.20	931	1664	1849	...	...	2602	1.10	41.8
143440.58+623002.5	2.144	2.154	...	1165	2340	2845	1639	4414	3362	5.70	42.2
143705.63+403231.5	3.075	3.071	21.04	453	...	...	...	...	1001	0.70	41.7
143725.05+351048.6	2.332	2.332	...	342	1864	1543	1417	...	...	0.50	41.3
150426.11+214559.4	2.243	2.241	...	891	2029	2243	1841	3192	2419	2.10	41.8
153005.44+174725.9	2.105	2.114	...	92	...	569	851	2562	1677	3.80	42.0
161433.15+533249.4	3.021	3.017	21.24	814	...	...	1287	...	2312	1.80	42.1
164850.00+272605.5	2.848	2.853	21.60	284	674	3729	599	...	2293	1.60	42.0
222028.54+000531.6	2.737	2.733	21.20	398	...	1189	...	...	2476	1.80	42.0
222555.71+183350.4	2.592	2.592	20.75	550	1046	...	...	...	2261	0.80	41.6

**Note.** First column: J2000 coordinates of the quasars. Second column: quasar emission redshift. Third column: ghostly absorber absorption redshift. Fourth column: logarithm of H I column density. Here we only report the H I column densities of the systems for which at least one extra Lyman series transition other than Ly $\alpha$  is observed. Columns 5 to 10 list the rest EW (in milliangstrom) of the Fe II  $\lambda$ 1608, Fe II  $\lambda$ 2382, Fe II  $\lambda$ 2600, Al II  $\lambda$ 1670, Mg II  $\lambda$ 2796, and C II  $\lambda$ 1334 absorption lines, respectively. The quasar flux (in  $10^{-17}$  erg s $^{-1}$  cm $^{-2}$  Å $^{-1}$ ) and the logarithm of its luminosity at 1500 Å are listed in columns 11 and 12.

**Table 2**  
Search Results

Plate-MJD-Fiber	$z_{\text{QSO}}$	S-1	S-2	S-3	S-4	S-5	Ghostly Absorbers
3589-55186-0218	2.05956	S-1	S-2	...	...	...	...
3589-55186-0282	2.56000	S-1	S-2	S-3	S-4	...	...
3589-55186-0364	2.14973	S-1	...	...	...	...	...
3589-55186-0942	2.11600	S-1	S-2	...	...	...	...
3589-55186-0982	2.34500	S-1	...	...	...	...	...

**Note.** First column: Plate, MJD, and Fiber ID of the quasars. Second column: Quasar redshift. The third to eighth columns show the subsamples each quasar is a member of. Table 2 is published in its entirety in the electronic edition of the *Astrophysical Journal*. A portion is shown here for guidance regarding its form and content.

(This table is available in its entirety in machine-readable form.)

mentioning that we first checked and found that by cross-correlating this absorption template with the spectra of the DLAs from the Paper I sample, the cross-correlation function (CCF) almost always has a peak with  $\geq 5\sigma$  significance at the DLA redshift. Therefore, we take into account only those systems from the  $S_{\text{QSO}}^4$  sample for which the CCF has a maximum with  $\geq 5\sigma$  significance. With this constraint on the  $S_{\text{QSO}}^4$  sample, most false-positive detections are excluded and we are left with 1446 systems. We call this new sample the  $S_{\text{QSO}}^5$  sample. By visually inspecting all spectra from the  $S_{\text{QSO}}^5$  sample, we could identify 30

ghostly absorbers (see Table 1). The remaining systems are mostly LLSs (with  $\log N(\text{H I}) < 19.0$ ) for which the Ly $\alpha$  absorption is also observed in the spectra. All S1QSO to S5QSO samples are available in machine-readable format. An extract of the full table is shown in Table 2.

## 2.2. Constraining H I Column Densities

In this section, we present different approaches used to constrain the H I column densities of the ghostly absorbers.

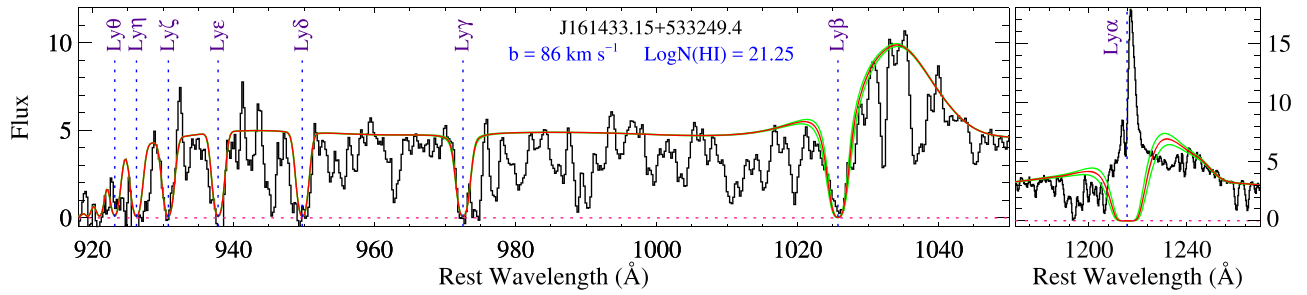


**Figure 2.** Example of a simultaneous Voigt profile fit (red curve) to the Lyman series absorption lines in the spectrum of quasar SDSS J161433.15+533249.4 with  $z_{\text{abs}} = 3.017$ . The green curves show the profile variations corresponding to  $\pm 0.1$  dex in the H I column density measurement. Note that no strong Ly $\alpha$  absorption is seen in the Ly $\alpha$  spectral region (right-hand panel).

### 2.2.1. Ghostly Absorbers with Lyman Series Absorption

Although ghostly absorbers reveal almost no Ly $\alpha$  absorption in the spectra, one could still use the absorption from other Lyman series transitions to constrain  $N(\text{H I})$  provided the redshift of the DLA is high enough that the Lyman series are covered by the SDSS spectrum. We will see higher Lyman series absorption because (1) since we see strong metal absorption lines, the cloud most certainly covers the QSO continuum completely, and (2) the continuum-to-emission line ratio is large for all Lyman series lines except Ly $\alpha$ . We note that our best H I column density measurements of ghostly absorbers are achieved through the fitting of the Lyman series absorption lines.

The minimum DLA redshift at which at least one more H I transition other than Ly $\alpha$  falls on the observed spectral window is  $z_{\text{abs}} \sim 2.55$  for the BOSS spectra. Thirteen (out of 30) of our ghostly absorbers satisfy this criterion. To constrain  $N(\text{H I})$  of these DLAs, we simultaneously fit all absorption lines from the H I Lyman series that are available in the spectra. An example of such a fit is shown in Figure 2, and the fits of the remaining systems are presented in the Appendix. The parameters of the fit are listed in Table 1. We show in Figure 3 the H I column density distribution of the ghostly absorbers measured from the fit to the Lyman series absorption lines. As shown in this figure, the majority of the systems with at least one transition other than Ly $\alpha$  available in the spectrum have H I column densities larger than  $\log N(\text{H I}) = 21.0$ .

### 2.2.2. Multicomponent Fit on Lyman Series Absorption

In this section, we explore the possibility that our ghostly absorbers are not single-component structures and that they are made up of several adjacent LLSs that may reduce the total  $N(\text{H I})$  column density. Since the signal-to-noise ratios (S/Ns) of the individual spectra in the Lyman series spectral region are low, we do this exercise on the stacked spectrum, which has a better S/N. Section 3.4 describes how the stacked spectrum is constructed. Our best single-component fit on the Lyman series absorption lines in the stacked spectrum is achieved for  $b = 105 \text{ km s}^{-1}$  and  $\log N(\text{H I}) = 21.0$  (see the upper panel in Figure 4).

We then perform a multicomponent fit with  $n$  ( $= 5, 10, 20, 30$ ) components. The  $b$ -value of each component is fixed to  $b = 10 \text{ km s}^{-1}$ , and the components are uniformly distributed over the velocity width of  $\Delta V = 250 \text{ km s}^{-1}$ . We derive  $\Delta V$  by fitting a Gaussian function on the Fe II  $\lambda 1608$  and Al II  $\lambda 1670$  absorption lines. For simplicity, we assume similar column densities for all components. The results of our multicomponent fits are shown in Figure 4. As shown in this figure, the fit with

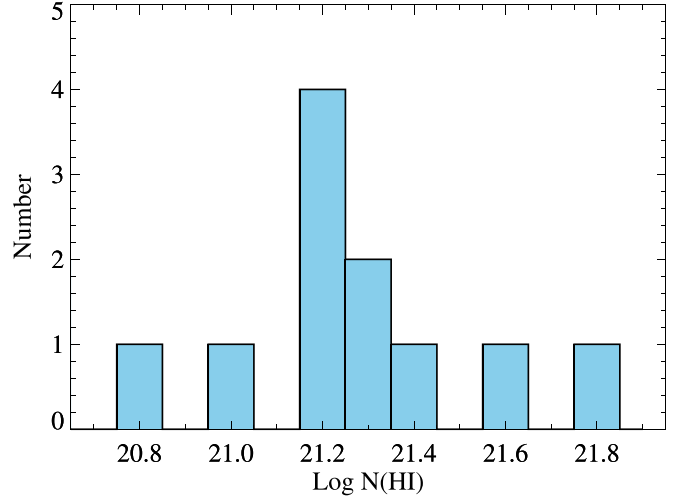


**Figure 3.** H I column density distribution for the ghostly absorbers, measured from the Voigt profile fits to the Lyman series absorption lines excluding Ly $\alpha$  (see the text).

five components is clearly ruled out because, except for Ly $\beta$ , the model underestimates the optical depth of the absorption from other Lyman series lines.

We found that the lowest number of components for which a rather satisfactory reconstruction of the observation is achieved is  $n = 10$ . In this case, each component has  $\log N(\text{H I}) = 19.60$ , and the total H I column density is  $\log N(\text{H I}) = 20.60$ . We also tried 20- and 30-component structures, which resulted in almost the same total H I column density of  $\log N(\text{H I}) = 20.40$ . Careful inspection of the Ly $\beta$  absorption lines in Figure 4 shows that the wings of the Ly $\beta$  absorption line are better reproduced with the single-component fit and  $\log N(\text{H I}) = 21.0$ . Although uncertain, the multicomponent fits show that the H I column densities are robustly larger than  $\log N(\text{H I}) = 20.40$ .

### 2.2.3. Ghostly Absorbers with Shallow Ly $\alpha$ Absorption Dip

As mentioned in Section 2.2.1, when the redshift of the DLA is below  $z_{\text{abs}} \sim 2.55$ , only the Ly $\alpha$  spectral region falls in the observed spectral window. This is the case for 17 (out of 30) of our ghostly absorbers. In these systems, the absence of absorption from neutral hydrogen makes it almost impossible to measure the H I column density. However, in seven of our ghostly absorbers, a shallow absorption dip is seen at the expected position of the DLA absorption. This shallow absorption dip is actually a ghostly signature of an otherwise strong Ly $\alpha$  absorption. This absorption dip can help us



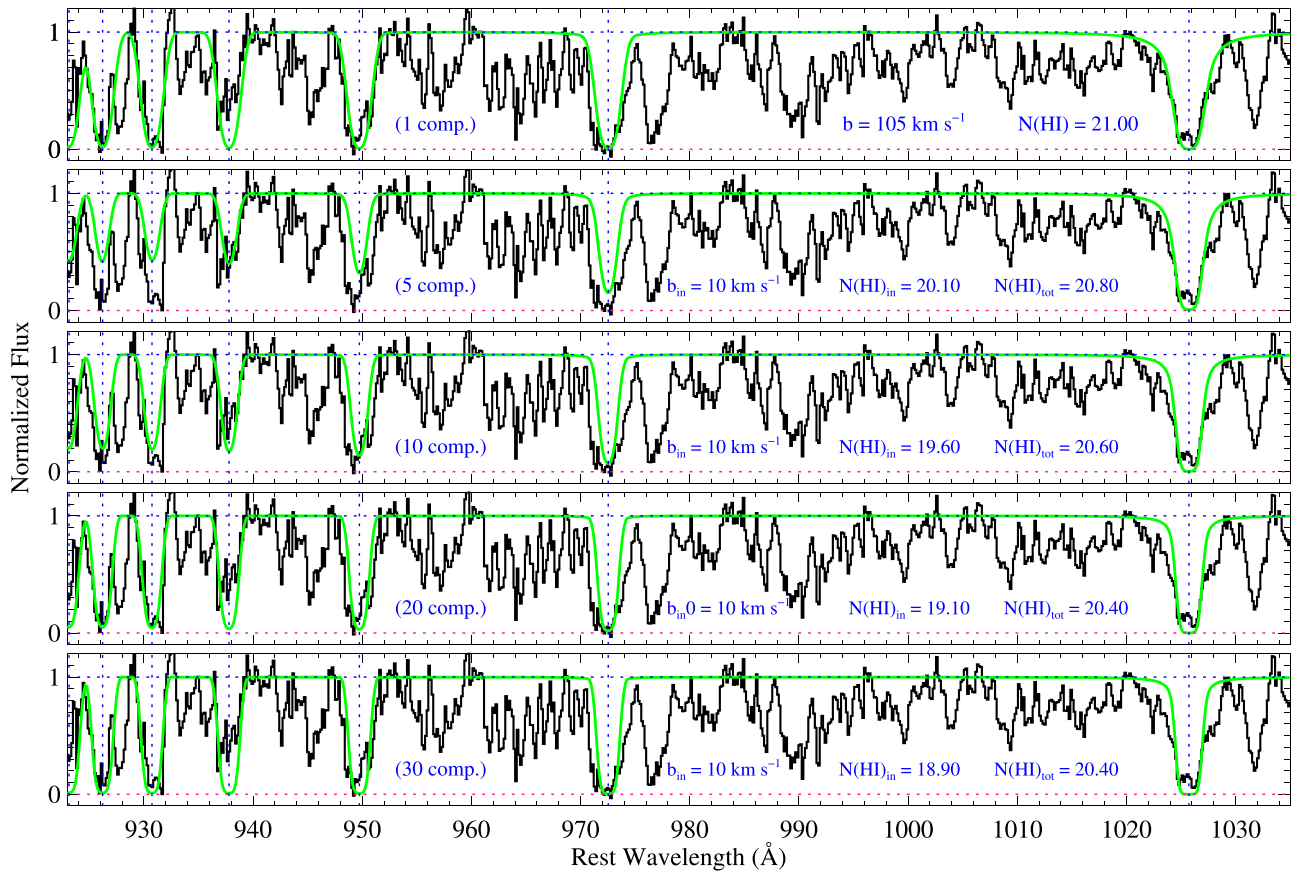


**Figure 4.** Multicomponent Voigt profile fit to the Lyman series absorption lines in the stacked spectrum of our ghostly absorbers. In each subpanel, the number of components, the  $b$ -value and  $N(\text{H I})$  of each component, and the total  $N(\text{H I})$  are also shown. In multicomponent fits, the individual components are spread over the velocity width of  $\Delta V = 250 \text{ km s}^{-1}$  obtained from a Gaussian fit to the low-ionization species.

constrain the H I column densities, as discussed in detail by Fathivavsari et al. (2017). Below, we briefly explain the technique.

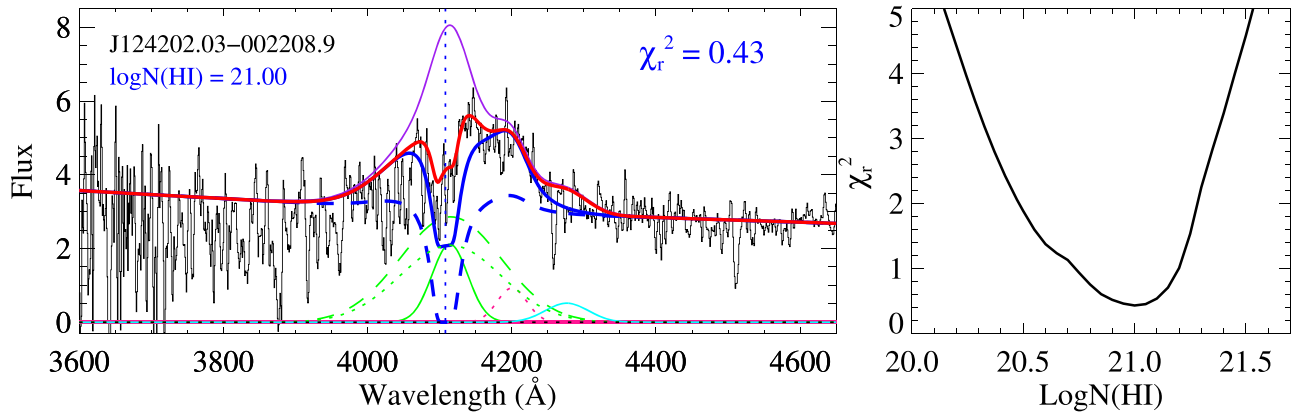
The technique is based on predicting the amount of neutral hydrogen that is needed to reproduce the shape of the shallow dip seen in the Ly $\alpha$  spectral region. To estimate the H I column density, we model the DLA absorption and the broad Ly $\alpha$  and N V and Si II emission lines. To this end, a series of models with fixed  $N(\text{H I})$  (varying from  $\log N(\text{H I}) = 19.0$  to 22.5) is constructed. In each of these models, the amplitude, the FWHM, and the redshift of the broad Ly $\alpha$  and N V emission line components are set as free parameters. Each of the broad Ly $\alpha$  and N V emission lines is assumed to have two components (Fathivavsari et al. 2017). The covering factor of the narrow component of the Ly $\alpha$  emission is fixed at 0.0, while that of the broad component is set as a free parameter. The redshift of the DLA is also fixed to that obtained from the low-ionization metal absorption lines.

Figure 5 shows an example of a reconstruction of the quasar spectrum around the Ly $\alpha$  spectral region. The broad (narrow) components of the Ly $\alpha$  and N V emission lines are shown as dashed (solid) green and pink curves. The Si II emission line of the quasar is shown as a cyan curve. The purple curve shows the reconstructed quasar spectrum, which is the combination of the quasar continuum (a power-law function) and all green, pink, and cyan dashed and solid curves. We found that the best match between the model and the observation is achieved when the partial coverage of the broad component of the BLR Ly $\alpha$

emission is 30%. The dotted green curve actually shows the corresponding 70% leaked Ly $\alpha$  emission from the BLR. Note that the covering factor of the narrow component of the BLR Ly $\alpha$  emission line is assumed to be 0%. The dashed blue curve is the combination of the quasar continuum, the dashed pink curve plus a DLA absorption profile with  $\log N(\text{H I}) = 21.00$ . The solid blue curve shows the combination of the dashed blue curve and dotted green curve. The final fit, which is overplotted as a red curve on the observed spectrum, is achieved by adding the solid green curve to the solid blue curve. The Si II emission line (the cyan curve) is also included in the red curve. The right-hand panel in Figure 5 shows the reduced  $\chi^2$  values for different H I column densities. The  $\chi^2$  map in Figure 5 implies that the hydrogen column density is  $\log N(\text{H I}) \sim 21.0$ . The fits of the remaining systems are shown in the Appendix. It must be noted that these estimates of H I column densities are highly uncertain compared to the ones measured from the fits to the Lyman series (see Section 2.2.1).

#### 2.2.4. Ghostly Absorbers with No Signature of H I Absorption

Ten (out of 17) of the ghostly absorbers with  $z_{\text{abs}} < 2.55$  reveal no signature of the Ly $\alpha$  absorption in the spectra. For these systems, the methods described in the two previous sections are not applicable. However, since at  $z_{\text{abs}} < 2.55$  the Mg II doublet falls in the observed spectral window in the BOSS spectra, one could exploit the strength of the Mg II  $\lambda 2796$  absorption line to *at least* infer whether these absorbers are DLAs (Rao et al. 1995, 2006; Ellison et al. 2009; Berg et al. 2017). Rao et al. (2006)



**Figure 5.** Example of reconstruction of the observed spectrum around the DLA absorption spectral region (see the text for the full description of the plots).

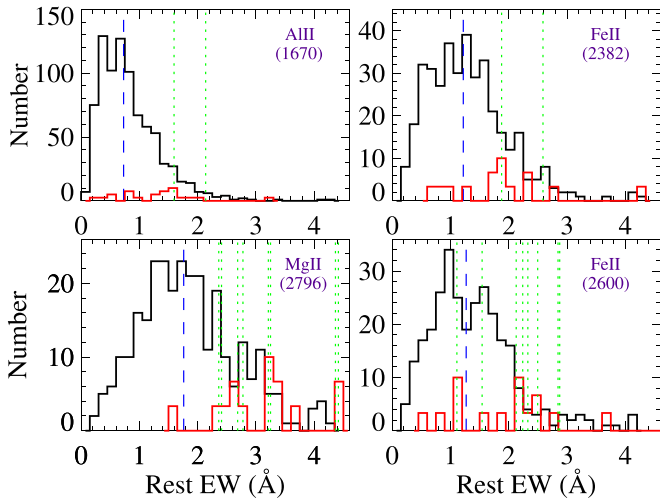


**Figure 6.** Rest EW distributions of the Al II  $\lambda 1670$ , Fe II  $\lambda 2382$ , Fe II  $\lambda 2600$ , and Mg II  $\lambda 2796$  absorption lines for the ghostly absorbers (red histograms) and intervening DLAs (black histograms) with  $z_{\text{abs}} = 2.3 \pm 0.2$  and  $\log N(\text{H I}) = 20.50 \pm 0.20$  (comparable to the mean values of  $z_{\text{abs}}$  and  $\log N(\text{H I})$  in our ghostly absorber sample) from Noterdaeme et al. (2012). The blue vertical dashed line shows the mean of the EWs of intervening DLAs. The green vertical dotted lines mark the EWs of the ghostly absorbers that reveal no signature of Ly $\alpha$  absorption (see the text). We note that, for the sake of a better illustration, the red histograms are normalized such that their peak value is at 10.

studied 197 Mg II systems with  $z_{\text{abs}} < 1.65$  and found that  $36\% \pm 6\%$  of the absorbers with the Mg II  $\lambda 2796$  and Fe II  $\lambda 2600$  rest EWs above  $0.5 \text{ \AA}$  are DLAs. From their Table 1, the median rest EWs of Mg II  $\lambda 2796$  and Fe II  $\lambda 2600$  for the DLAs in their sample are  $1.9 \text{ \AA}$  and  $1.3 \text{ \AA}$ , respectively.

We have measured the rest EWs of Mg II  $\lambda 2796$  and Fe II  $\lambda 2600$  absorption lines for the ghostly absorbers in our sample (see Table 1). In the two (out of 10) systems, the Mg II absorption lines are contaminated by noise. The EWs of the Mg II  $\lambda 2796$  absorption line in the remaining eight systems with clean Mg II absorption are all larger than  $2.4 \text{ \AA}$ , so they are higher than the median rest EW of this absorption line in the Rao et al. (2006) sample (see above). Moreover, the rest EWs of Fe II  $\lambda 2600$  in all but one (toward J090424.08+560205.4) of these eight systems are larger than the median rest EW of the Fe II  $\lambda 2600$  absorption line in the Rao et al. (2006) sample. We plot, in Figure 6, the rest EW distributions of the Mg II  $\lambda 2796$  and Fe II  $\lambda 2600$  absorption lines in our ghostly absorbers (red

histograms) and in the intervening DLAs (black histograms) with  $z_{\text{abs}} = 2.3 \pm 0.2$  and  $\log N(\text{H I}) = 20.50 \pm 0.20$  from Noterdaeme et al. (2012). As shown in this figure, all eight of our Mg II EW measurements are larger than the median of the distribution. These indications imply that these eight systems are highly likely to be DLAs. We also note that the EWs of Mg II  $\lambda 2796$  absorption lines in all our ghostly absorbers with Mg II measurements are much larger than the median of the EW of this absorption line in the intervening LLS (i.e.,  $(\text{EW})_{\text{LLS}} < 1.0 \text{ \AA}$ ; Nestor et al. 2006).

In order to assess whether the two remaining systems (with no Mg II  $\lambda 2796$  and Fe II  $\lambda 2600$  measurements available) could also be DLAs, we make a comparison of the rest EWs of Al II  $\lambda 1670$  and Fe II  $\lambda 2382$  in the two systems with those of the intervening DLAs from Noterdaeme et al. (2012). The results are shown in the upper panel of Figure 6. As shown in this figure, the rest EW of Al II  $\lambda 1670$  (Fe II  $\lambda 2382$ ) is  $\sim 2.2$  ( $\sim 1.6$ ) times larger than the median rest EW of Al II  $\lambda 1670$  (Fe II  $\lambda 2382$ ) of the intervening DLAs. The high EW of these absorption lines hints at the possibility that these absorbers could also be DLAs.

### 2.3. Ly $\beta$ and C IV Absorption in Ghostly Absorbers

Since the DLA absorption troughs in ghostly absorbers are almost fully filled with the leaked Ly $\alpha$  emission from the BLR (and NLR), one would expect the corresponding leaked Ly $\beta$  emission from the BLR to also fill the Ly $\beta$  absorption trough in the spectra. However, in all ghostly absorber candidates for which the Ly $\beta$  spectral region is observed, the Ly $\beta$  absorption is clearly visible. Here we demonstrate that this is because, in the spectrum, the ratio of the continuum to the Ly $\beta$  emission is larger than the ratio of the continuum to the Ly $\alpha$  emission.

For this, we use the ghostly absorber toward the quasar J0222+0005, which reveals a shallow dip in both the Ly $\alpha$  spectral region (which is a signature of a DLA absorption) and the Ly $\beta$  absorption. We first follow the technique described in Section 2.2.3 and determine the H I column density from the Ly $\alpha$  absorption dip. To properly fit the shallow dip, we require the partial coverage of the BLR to be  $\sim 0.7$ . We then assume that the Ly $\beta$ /Ly $\alpha$  emission line ratio is  $\sim 0.2$  (Martin 1988), and consequently we fit the Ly $\beta$  absorption by taking into account a partial coverage of 0.7 for the BLR. The result is shown in Figure 7. As shown in this figure, the Ly $\beta$  absorption line is only slightly elevated and is clearly visible in the spectrum despite the highly elevated DLA absorption trough.

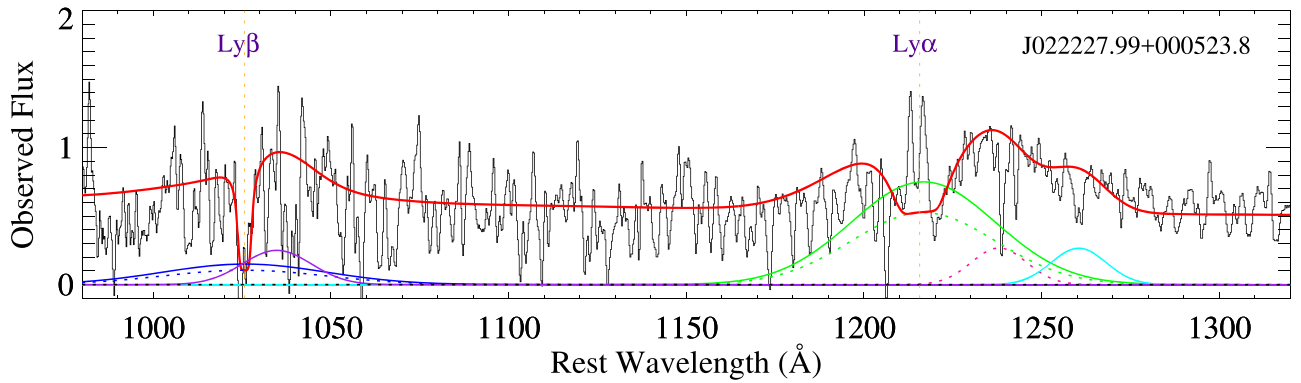


**Figure 7.** Fit to the  $\text{Ly}\alpha$  and  $\text{Ly}\beta$  absorption spectral regions. The green (blue) solid curve shows the BLR  $\text{Ly}\alpha$  ( $\text{Ly}\beta$ ) emission, and the dotted green (blue) curve shows the fraction of this emission that leaks because of the partial coverage of the DLA cloud. The  $\text{Ly}\beta/\text{Ly}\alpha$  ratio is assumed to be 0.2. The dotted pink curve and the solid cyan curve show the N V and Si II emission lines of the quasar. The BLR O VI emission is shown as a solid purple curve. See the text for the full description.

The low S/N of the spectrum does not allow for accurate measurement of the flux in the  $\text{Ly}\beta$  absorption trough. High S/N and higher resolution spectra of our ghostly absorbers would be needed to better estimate the flux at the bottom of the  $\text{Ly}\beta$  absorption line and correspondingly determine more accurately the  $\text{Ly}\beta/\text{Ly}\alpha$  ratio.

We also probed the partial coverage of the BLR by the high-ionization phase of the cloud, using the C IV doublet absorption lines. In most of our systems, the C IV absorption lines are very strong, and the two components of the doublet are heavily blended. Nevertheless, seven systems reveal well-separated components to allow for a successful Voigt profile fitting of the doublet. In these systems, we could conduct single-component fits on the C IV absorption lines without invoking partial coverage. The lack of partial coverage could be easily explained by the fact that the high-ionization phase of the cloud is more extended than the low-ionization or neutral phase of the cloud. However, we could still get a satisfactorily good fit even if we remove a residual flux of up to 15% from the bottom of the C IV absorption lines. This would imply that the observed C IV absorption lines in these systems are not inconsistent with the presence of partial coverage. Higher resolution spectra would be needed to properly tackle this issue.

### 3. Results

In Paper I, we conjectured that eclipsing DLAs with strong  $\text{Ly}\alpha$  emission arise in smaller and denser clouds and possibly closer to the AGN. Here, we would like to ascertain this conclusion using ghostly absorbers. In this section, we characterize the ghostly absorber sample and then compare their properties with those of the eclipsing DLAs. We note that in Paper I we defined two kinds of eclipsing DLAs: (1) eclipsing DLAs with weak, narrow  $\text{Ly}\alpha$  emission (i.e., the integrated flux or IF of the narrow  $\text{Ly}\alpha$  emission is  $< 20 \times 10^{-17} \text{ erg s}^{-1} \text{ cm}^{-2} \text{ Å}^{-1}$ ) in their DLA troughs, and (2) eclipsing DLAs with strong, narrow  $\text{Ly}\alpha$  emission (i.e., IF  $\geq 20 \times 10^{-17} \text{ erg s}^{-1} \text{ cm}^{-2} \text{ Å}^{-1}$ ). Here, we also consider these two kinds of eclipsing DLAs separately.

#### 3.1. Kinematics

For each quasar in our ghostly absorber sample, we remeasure the emission redshift by conducting Gaussian fits on the He II, C III, and Mg II emission lines. These emission

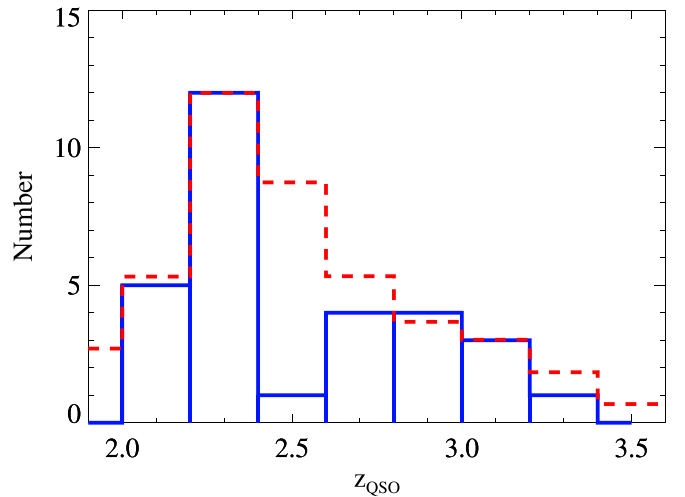


**Figure 8.** The blue histogram shows the distribution of the quasar redshifts for the ghostly absorber sample. For the sake of comparison, the redshift distribution for all DR12 quasars with  $z_{\text{QSO}} > 2.0$  is also shown as a red dashed histogram.

lines are good redshift indicators as their statistical shift with respect to the quasar systemic redshift is small (Hewett & Wild 2010). The redshift distribution of ghostly absorbers is shown in Figure 8 as a blue histogram. For the sake of comparison, the redshift distribution for all DR12 quasars with  $z_{\text{QSO}} > 2.0$  is also shown in Figure 8 as a red dashed histogram. There seems to be a deficit of systems in the redshift range  $2.4 < z_{\text{QSO}} < 2.6$ . Apart from this, the redshift distribution of ghostly absorbers seems to follow that of the full DR12 quasars, implying that there is no preferred redshift for the occurrence of ghostly absorbers. Moreover, in contrast to the redshift distribution of eclipsing DLAs, which shows some excess of quasars at  $3.0 < z_{\text{QSO}} < 3.2$  (see Figure 9 in Paper I), in the redshift distribution of ghostly absorbers, no such excess is seen over this redshift range.

Figure 9 shows the distribution of the velocity offset between the ghostly absorbers and the quasars. Here, a positive velocity offset means the DLA is infalling toward the quasar. Although eclipsing DLAs show a tendency for positive DLA–QSO velocity offset (indicating inflow toward the quasars; see Figure 10 in Paper I), ghostly absorbers seem to be equally distributed around the zero-velocity offset.

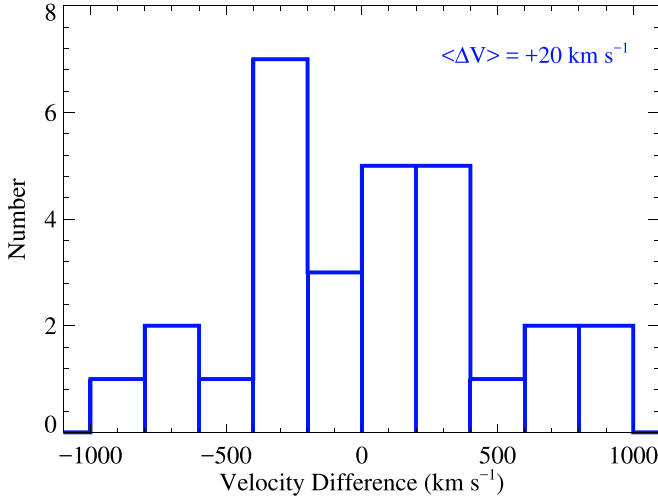


**Figure 9.** Distribution of the velocity offset between ghostly absorbers and their quasars. It seems that ghostly absorbers are equally distributed around the zero velocity. The ghostly absorber redshifts are measured by fitting the absorption lines from the low-ionization species. The quasar emission redshifts, on the other hand, are measured from the Gaussian fits applied on the He II and/or Mg II emission lines available in the quasars' spectra.

### 3.2. Reddening due to Dust

In this section, we employ different techniques to investigate the reddening of the quasar spectra that is due to the presence of dust in our ghostly and eclipsing DLAs.

#### 3.2.1. Reddening Estimates Based on Spectral Index Distributions

By examining the difference in the spectral indices of the spectra of the ghostly and eclipsing DLA quasars, one can probe the reddening of the quasar spectra that is due to dust in these absorbers (Murphy & Liske 2004; Wild & Hewett 2005; Wild et al. 2006; Ellison et al. 2010; Kaplan et al. 2010). The first step in this approach is to determine the spectral index,  $\alpha$ , defined as  $f_\lambda \propto \lambda^{-\alpha}$ , by fitting a power law to the regions in the spectrum free from emission and absorption lines. The presence of dust in a DLA would extinguish the quasar emission, leading to smaller values of the spectral index. Following the approach described in Ellison et al. (2010), we fit a power law on the spectra of each of our quasars. The distribution of the spectral indices,  $\alpha$ , is shown in Figure 10. As can be seen from this, quasars with eclipsing DLAs with strong emission have a smaller median  $\alpha$  compared to what is seen in eclipsing DLAs with weak emission. The lowest median value of  $\alpha$  belongs to the ghostly absorber sample, implying that quasars behind these DLAs are the reddest.

#### 3.2.2. Reddening Estimates Based on Quasar Colors

We plot in Figure 11 the  $\Delta(g-i)$  colors as a function of quasar redshift (left panel) for the sample of ghostly absorbers (red filled squares) and eclipsing DLAs with weak (blue filled circles) and strong (green triangles) Ly $\alpha$  emission in their troughs. The panel on the right gives the corresponding distribution for different-color bins. In this panel, the colored dashed lines show the median values of  $\Delta(g-i)$  for different samples. Consistent with the results obtained in Section 3.2.1, eclipsing DLAs with stronger emission have redder colors ( $\Delta(g-i) = 0.31$ ) than those with weaker emission ( $\Delta(g-i) = 0.48$ ), and ghostly absorbers exhibit the reddest color with  $\Delta(g-i) = 0.59$ .

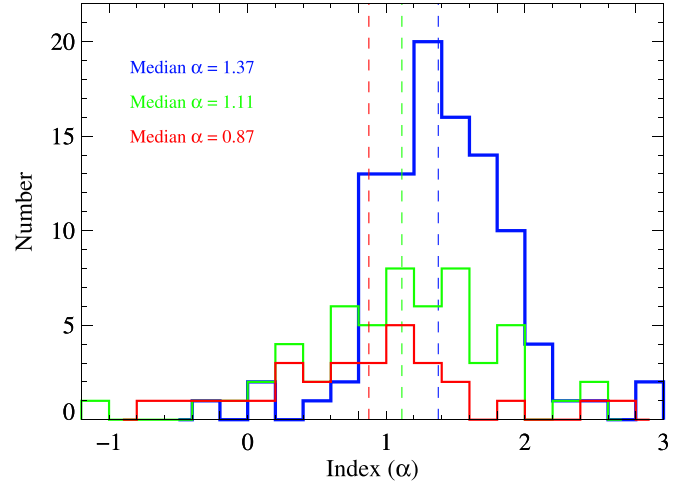


**Figure 10.** Distribution of power-law indices for the quasars behind ghostly absorbers (red histogram) and eclipsing DLAs with weak (blue histogram) and strong (green histogram) narrow Ly $\alpha$  emission in their troughs.

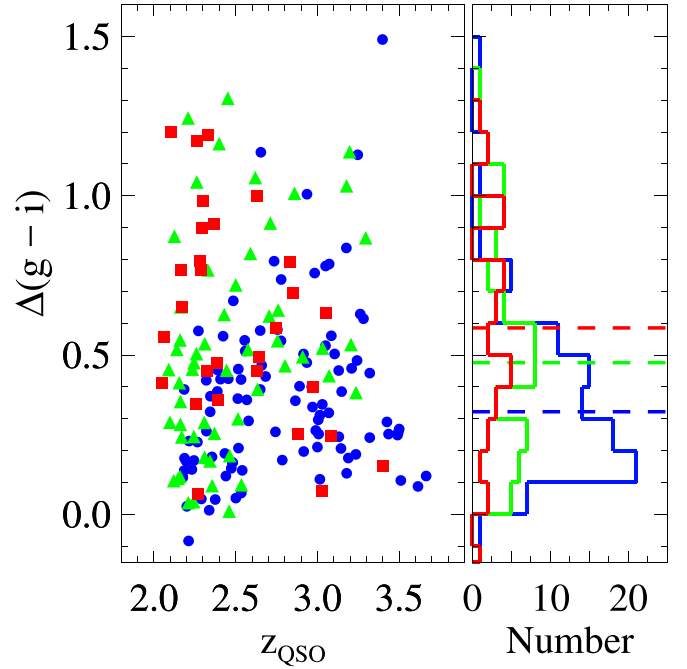


**Figure 11.**  $\Delta(g-i)$  color as a function of the quasar redshift (left-hand panel), and the  $\Delta(g-i)$  color distribution (right-hand panel) for the samples of ghostly absorbers (red filled squares and histogram) and eclipsing DLAs with weak (blue filled circles and histogram) and strong (green filled triangles and histogram) narrow Ly $\alpha$  emission in their troughs.

Using the SMC reddening law (Prevot et al. 1984; Khare et al. 2004),

$$A_\lambda = 1.39 \lambda^{-1.2} E(B - V), \quad (1)$$

we can determine  $E(B - V)_{(g-i)}$  from the observed  $\Delta(g - i)$  values. Taking  $\lambda_g$  and  $\lambda_i$  to be 4657.98 and 7461.01 Å, respectively, we find

$$E(B - V)_{g-i} = \Delta(g - i)(1 + z_{\text{abs}})^{-1.2}/1.506, \quad (2)$$

where  $z_{\text{abs}}$  is the redshift of the DLA. To convert to an  $A_{V(g-i)}$ , we use the standard definition  $A_V = R_V E(B - V)$  with  $R_V = 2.74$  (Gordon et al. 2003). Converting the observed  $\Delta$



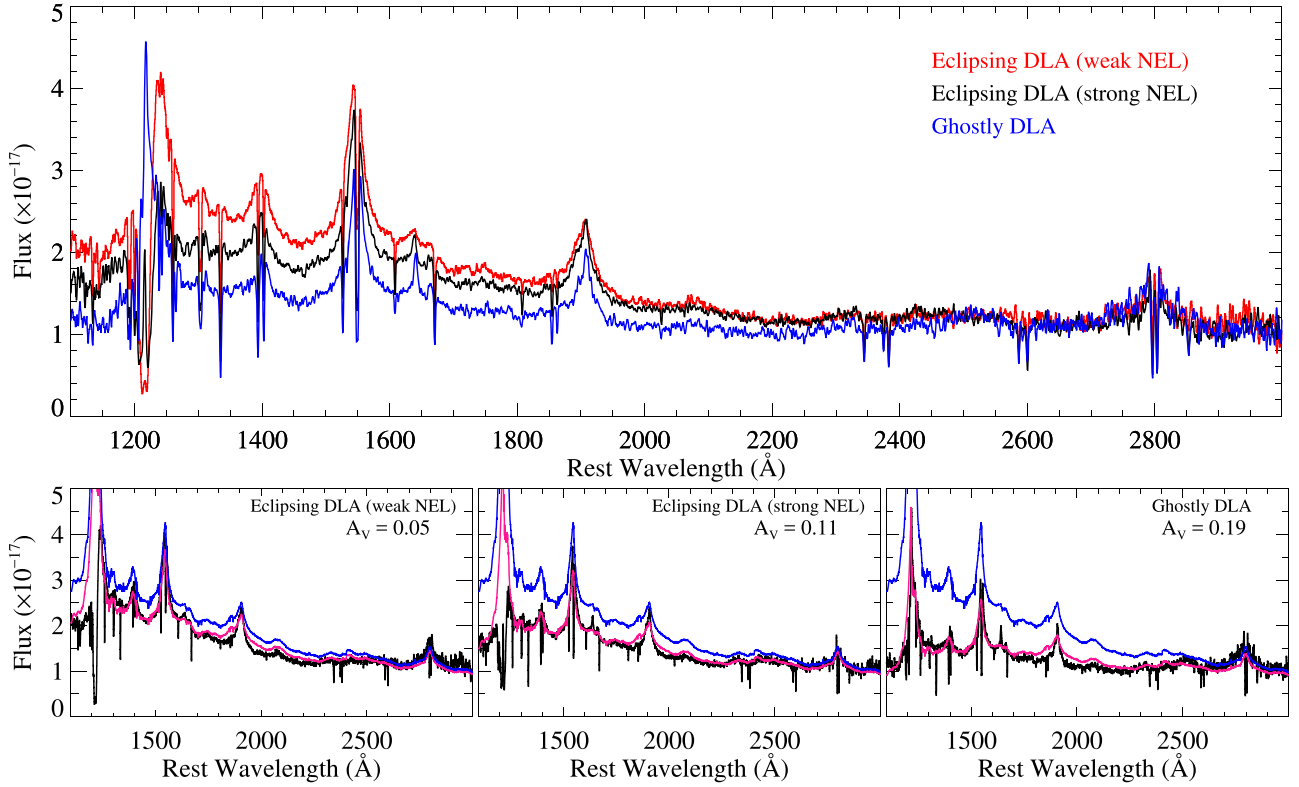


**Figure 12.** Upper panel: geometric mean composite spectra of ghostly (blue spectrum) and eclipsing DLAs with strong (black spectrum) and weak (red spectrum) narrow Ly $\alpha$  emission. Lower panels: geometric composite spectra of ghostly (right panel) and eclipsing DLAs with strong (middle) and weak (left) emission are shown in black. The blue spectrum in each subpanel is the template spectrum from Selsing et al. (2016), and the pink spectrum in each subpanel shows the reddened template spectrum. The flux is in  $\text{erg s}^{-1} \text{cm}^{-2} \text{\AA}^{-1}$ .

( $g-i$ ) to  $A_{V(g-i)}$ , we get median  $A_{V(g-i)} = 0.24, 0.19$ , and  $0.12$  for the ghostly and eclipsing DLAs with strong and weak emission, respectively.

### 3.2.3. Reddening Estimates Based on Geometric Mean Composite Spectra

The geometric mean composite spectra of ghostly (blue spectrum) and eclipsing DLAs with strong (black spectrum) and weak (red spectrum) narrow Ly $\alpha$  emission are shown in the upper panel of Figure 12. These composite spectra are used to estimate the extinction due to dust in these absorbers. We use the geometric mean to create the composite spectra because the geometric mean of a set of quasar spectra preserves the average power-law index of the spectra (York et al. 2006).

We use the template-matching technique to measure the extinction,  $A_V$  (Fitzpatrick & Massa 2007; Fynbo et al. 2013; Ranjan et al. 2018). The technique is based on iteratively reddening a template quasar spectrum (Selsing et al. 2016), using the SMC extinction curve (Gordon et al. 2003), until the reddened template best matches the observed spectrum. In this case, the observed spectrum,  $f_\lambda$ , can be represented as

$$f_\lambda = C_0 F_\lambda \left( \frac{\lambda}{\lambda_0} \right)^{\Delta\alpha} \cdot \exp\left(-\frac{1}{2.5 \log_{10}(e)} k_\lambda A_V\right), \quad (3)$$

where  $F_\lambda$  is the quasar template from Selsing et al. (2016),  $\Delta\alpha$  is the power-law slope relative to the intrinsic slope of the quasar template,  $k_\lambda$  denotes the SMC reddening curve,  $A_V$  is the V-band extinction, and  $C_0$  is an arbitrary factor, scaling the quasar intrinsic

flux. Using this equation to fit the observed spectra, we found  $A_V = 0.19 \pm 0.06, 0.11 \pm 0.07$ , and  $0.05 \pm 0.05$  for ghostly and eclipsing DLAs with strong and weak emission, respectively. For each composite, the uncertainty in  $A_V$  is estimated by adopting  $\Delta\alpha = \pm 0.2$  (see Krawczyk et al. 2015). Interestingly, these  $A_V$  values are consistent with the photometric measurement of extinction from Section 3.2.2. Since intervening absorbers are also present along the line of sight to the quasars used in constructing these composites, the possible presence of dust in these absorbers could in principle affect the shape of the continuum of the composite spectra. However, the consistency found between the spectroscopic and photometric measurements of extinction implies that the effect of dust extinction from intervening absorbers is negligible, and that the extinction predominantly arises in the ghostly and eclipsing DLAs.

Our results show that quasars behind ghostly absorbers are the reddest despite the lower HI column density in these absorbers (see Section 3.4.1).

### 3.3. Metals

Figure 13 shows the Kolmogorov–Smirnov (K-S) tests, comparing the rest EWs of Si II  $\lambda 1526$ , Fe II  $\lambda 1608$ , and C II  $\lambda 1334$  in the ghostly absorbers (red lines) and eclipsing DLAs with weak (blue lines) and strong (green lines) narrow Ly $\alpha$  emission in their DLA absorption troughs. As shown in the figure, the EWs are larger in the eclipsing DLAs with strong emission compared to what is observed in the eclipsing DLAs

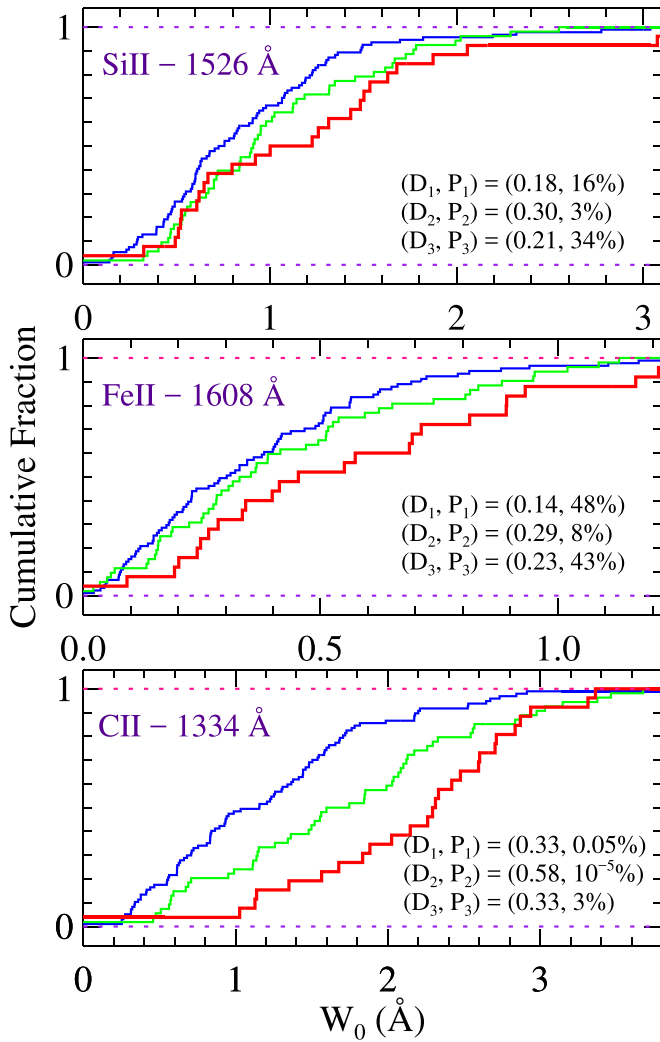


**Figure 13.** Kolmogorov–Smirnov tests comparing the rest EWs of Si II  $\lambda 1526$ , Fe II  $\lambda 1608$ , and C II  $\lambda 1334$  in the ghostly absorbers (red lines) and eclipsing DLAs with weak (blue lines) and strong (green lines) narrow Ly $\alpha$  emission in their troughs. The K-S test statistic,  $D$ , gives the maximum vertical distance between the two distributions, and the  $P$ -value is the probability that the two distributions are drawn from the same population.

with weak emission. Moreover, the largest EWs are observed in the ghostly absorbers. Higher EWs would imply that the absorbers are of higher metallicities or the DLAs are located in more turbulent regions.

As shown in Figure 13, the maximum distance parameter is the largest for C II  $\lambda 1334$  ( $D = 0.58$ ). We note that since the C II  $\lambda 1334$  and C II\*  $\lambda 1335$  absorption lines are almost fully blended with each other at the SDSS spectral resolution, the EW of the whole C II + C II\* absorption feature is taken as the EW of C II. Therefore, the stronger difference seen for C II is mainly due to the blending of this absorption line with the C II\*  $\lambda 1335$  absorption. If C II\* are stronger in ghostly absorbers, then the K-S test for Si II\* would be illuminating because stronger C II\* absorption could imply stronger absorption from Si II\*. Although the low S/N of the spectra does not allow us to perform the K-S test for this species, the Si II\* in the stacked spectra of eclipsing and ghostly absorbers clearly shows that ghostly absorbers have the strongest Si II\* absorption (see Section 3.4).

### 3.4. Normalized Median Composite Spectrum

In this section, we create a stacked spectrum of ghostly absorbers and then compare its absorption properties with those of the eclipsing DLAs with weak and strong Ly $\alpha$  emission. We also construct median composite spectra of the associated Super Lyman Limit System (SLLS; quasar absorption line systems with  $10^{19} \text{ cm}^{-2} \leq N(\text{H I}) \leq 10^{20.3} \text{ cm}^{-2}$ ) and intervening DLAs to compare with that of the ghostly absorbers.

#### 3.4.1. Comparison with Eclipsing DLAs

We first create a normalized stacked spectrum using the quasar spectra from our ghostly absorber sample. To create the stacked spectrum, all spectra are first shifted to the rest frame of the DLAs and then normalized. The final stacked spectrum is generated by median-combining these normalized spectra (Ellison et al. 2010; Rahmani et al. 2010). The aim of this section is to statistically look for differences between ghostly and eclipsing DLAs, by comparing the strength of the absorption lines in their stacked spectra. Here, we would like to test the hypothesis that ghostly absorbers are from the same population as eclipsing DLAs but with higher densities and closer distance to the quasars.

Figure 14 shows absorption from the Lyman series transitions for the composite spectra of ghostly absorbers (upper panels) and eclipsing DLAs with weak (lower panels) and strong (middle panels) Ly $\alpha$  emission in their troughs. The Voigt profile fits to the Lyman series absorption lines are overplotted on the observed spectra as red curves. The green curves show the uncertainty of  $\pm 0.10$  dex on the H I column density. The  $b$ -value increases from  $b = 53 \text{ km s}^{-1}$  in eclipsing DLAs with weak emission to  $b = 105 \text{ km s}^{-1}$  in ghostly absorbers. If we ascribe the line widths to turbulence, then higher  $b$ -values would imply that the cloud is exposed to a more turbulent region and perhaps is located closer to the quasar.

We determined the rest EWs of the absorption lines in the stacked spectrum of the ghostly absorbers using Gaussian fits (Fathivavsari et al. 2013). The results are summarized in Table 3. Figure 15 shows the empirical curve of growth constructed using the Si II absorption lines from the ghostly absorber composite spectrum (Prochaska 2006). The data from Si II\*, Fe II, and Al III are also included in Figure 15. The curve of growth analysis gives a metallicity of  $[\text{Si}/\text{H}] \sim -1.0$  for ghostly absorbers. This is similar to the metallicities estimated for the eclipsing DLAs with weak ( $\log Z/Z_{\odot} \sim -1.1 \pm 0.2$ ) and strong ( $\log Z/Z_{\odot} \sim -1.0 \pm 0.2$ ) Ly $\alpha$  emission. We note that the estimated column densities and metallicities are subject to the assumption of a single-component cloud. The large  $b$ -value shows that the cloud has a multicomponent structure. We therefore refer to these measurements as tentative estimates (Jenkins 1986).

Figure 16 presents the spectral regions of some important transitions in the stacked spectra of the ghostly and eclipsing DLAs. As shown in this figure, absorptions from the excited states of Si II and C II are detected in all three composites, but with different strengths. These absorption lines are the weakest in the eclipsing DLAs with weak emission (red curves), while they are the strongest in the ghostly absorbers (blue curves). Moreover, the strength of these absorption lines in the eclipsing DLAs with strong emission (black curves) is intermediate

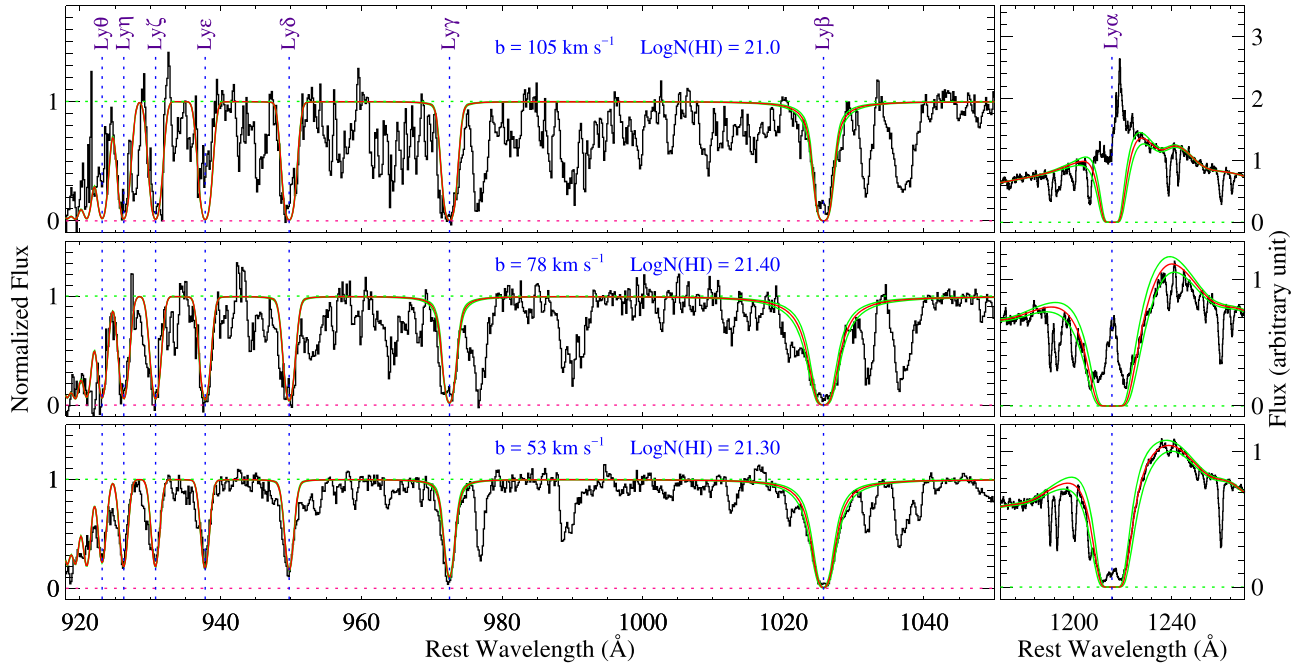


**Figure 14.** Voigt profile fits (red curves) on the Lyman series absorption lines in the composite spectra of the ghostly absorbers (upper panels) and the eclipsing DLAs with weak (lower panels) and strong (middle panels) Ly $\alpha$  emission in their troughs. The green curves show the  $\pm 0.1$  dex variations in the H I column density measurements.

**Table 3.**

Rest Equivalent Widths for the Three Composites in Milliangstroms

ID	$\lambda_{\text{lab}}$	Composite 1	Composite 2	Composite 3
N V	1238	$235 \pm 16$	$483 \pm 15$	$1071 \pm 11$
N V	1242	$120 \pm 5$	$446 \pm 28$	$667 \pm 9$
Si IV	1393	$585 \pm 13$	$953 \pm 18$	$1337 \pm 41$
Si IV	1402	$495 \pm 15$	$801 \pm 18$	$1222 \pm 14$
C IV	1548	$795 \pm 22$	$1420 \pm 12$	$2278 \pm 20$
C IV	1550	$633 \pm 21$	$1189 \pm 18$	$1342 \pm 20$
Al III	1854	$321 \pm 18$	$465 \pm 28$	$856 \pm 12$
Al III	1862	$201 \pm 24$	$370 \pm 23$	$642 \pm 21$
Si II	1260	$1036 \pm 15$	$1156 \pm 19$	$1248 \pm 10$
Si II	1304	$524 \pm 6$	$683 \pm 16$	$771 \pm 20$
Si II	1526	$692 \pm 18$	$890 \pm 19$	$1045 \pm 20$
Si II	1808	$240 \pm 16$	$298 \pm 12$	$200 \pm 40$
Si II*	1264	$71 \pm 6$	$303 \pm 22$	$790 \pm 50$
Si II*	1309	$33 \pm 13$	$113 \pm 16$	$330 \pm 20$
Si II*	1533	$15 \pm 3$	$164 \pm 14$	$470 \pm 50$
Fe II	1608	$430 \pm 7$	$462 \pm 13$	$364 \pm 15$
Fe II	2374	$804 \pm 46$	$785 \pm 33$	$657 \pm 100$
Fe II	2382	$1051 \pm 71$	$1021 \pm 25$	$972 \pm 200$
Al II	1670	$709 \pm 17$	$844 \pm 11$	$815 \pm 20$
C II	1334	$895 \pm 10$	$1220 \pm 15$	$1464 \pm 20$
C II*	1335	$232 \pm 13$	$455 \pm 17$	$657 \pm 20$

**Notes.** First column: ID of the species. Second column: rest wavelengths. Third column: rest EWs for the composite of eclipsing DLAs with weak narrow Ly $\alpha$  emission. Fourth column: rest EWs for the composite of eclipsing DLAs with strong narrow Ly $\alpha$  emission. Fifth column: rest EWs for the composite of ghostly absorbers.

between what is seen in ghostly absorbers and eclipsing DLAs with weak emission.

Fine structure levels can be populated by collisions, radiative pumping due to a local radiation field, and direct excitation by the cosmic microwave background (CMB) radiation (Silva & Viegas 2002; Wolfe et al. 2003, 2008; Srianand et al. 2005).

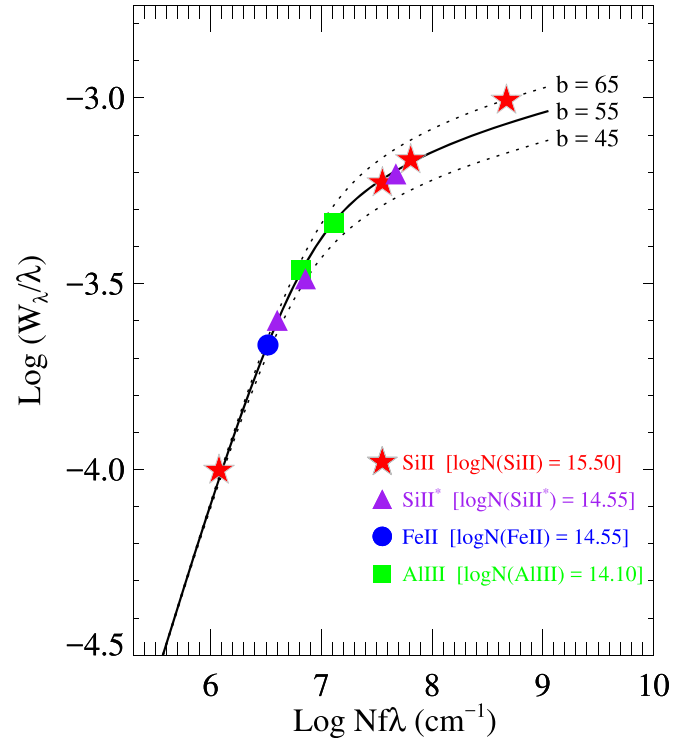


**Figure 15.** Empirical curve of growth constructed using the Si II absorption lines from the ghostly absorber composite spectrum. Column densities are from the weak transitions, and EWs are from Table 3.

However, direct excitation by the CMB radiation is negligible for Si II because the fine structure levels in Si II are so far apart from each other. The pattern seen in the strength of the Si II\* and C II\* absorption lines in the three composites (see Figure 16) implies that the gas is progressively getting denser or closer to the quasar as one goes from the eclipsing DLAs

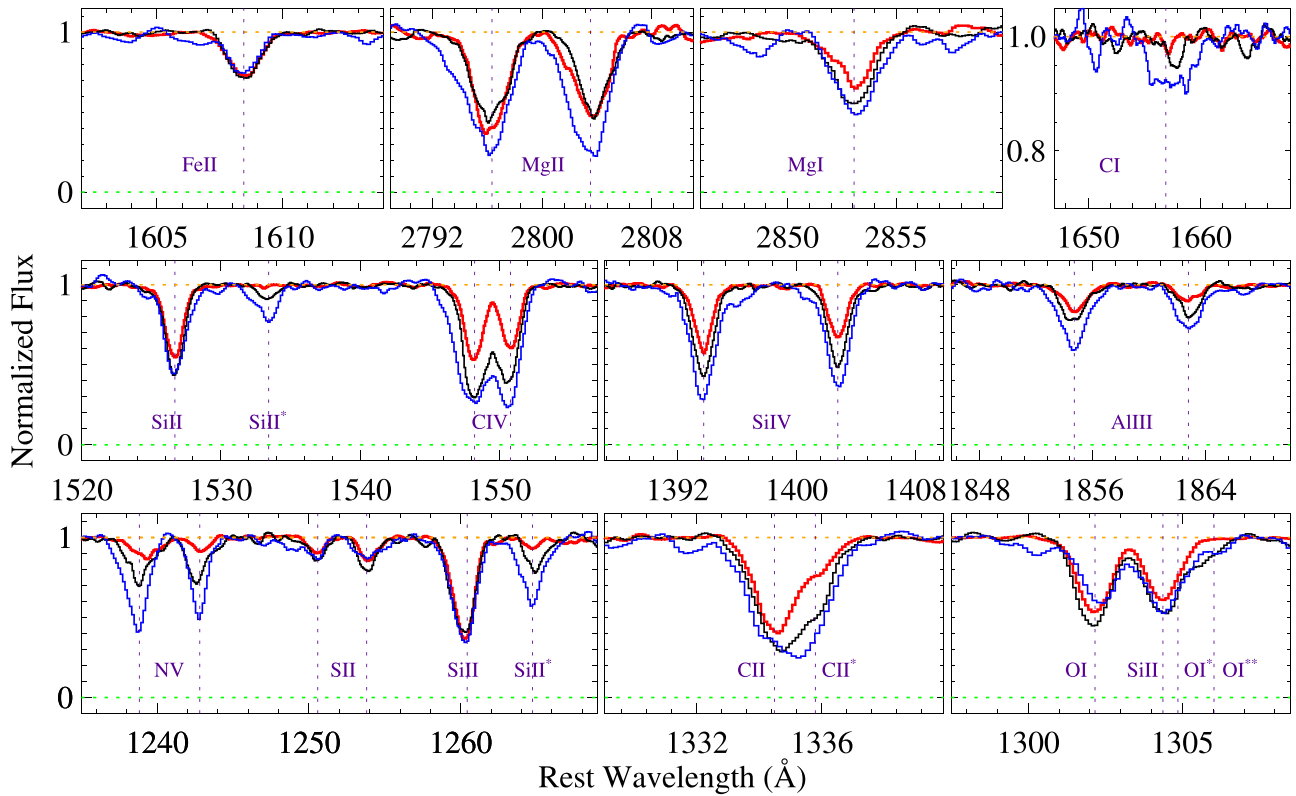


**Figure 16.** Some important transitions detected in the composite spectra of ghostly absorbers (blue curves) and eclipsing DLAs with weak (red curves) and strong (black curves) narrow Ly $\alpha$  emission.

with weak emission to ghostly absorbers. Higher resolution spectra of the ghostly and eclipsing DLAs would in principle allow us to disentangle the effects of higher gas density and proximity to the quasar.

As shown in Figure 16, although the O I\* absorption is fully blended with the Si II absorption at the SDSS spectral resolution, the O I\*\* absorption is clearly detected in both the eclipsing DLAs with strong emission and ghostly absorbers. The C I and Mg I absorptions are also detected in all three composites. However, due to the low S/N, the C I detection in the composite of eclipsing DLAs with weak emission is tentative. The detection of the C I and Mg I absorption in ghostly absorbers implies that the density of the gas should be high. While C I is known to be a good tracer of H<sub>2</sub> (Noterdaeme et al. 2018), the composite spectrum of ghostly absorbers does not show any signature of H<sub>2</sub>. However, we found an upper limit of  $10^{18} \text{ cm}^{-2}$  for the column density of H<sub>2</sub> in individual systems, which is standard in DLAs.

Similar to the Si II and C II excited state transitions, high-ionization species (i.e., NV, C IV, and Si IV) also exhibit the strongest absorptions in ghostly absorbers and the weakest absorptions in eclipsing DLAs with weak emission. This trend is also seen in the Al III absorption lines. Among the high-ionization species, the NV absorption shows the highest difference in the three composites. For example, the EW of the NV  $\lambda 1238$  absorption in ghostly absorbers is a factor of  $\sim 4.4$  ( $\sim 2.1$ ) higher than in eclipsing DLAs with weak (strong) emission. Stronger NV absorption could be attributed to higher metallicity (Ellison et al. 2010) or a higher level of ionization (Fox et al. 2009; Perrotta et al. 2016). However, the similar metallicities of the three composites, along with the fact that our ghostly absorbers have smaller H I column densities, hint at

the possibility that the stronger NV absorption in ghostly absorbers is mainly due to the higher level of ionization in the external layers of these gas clouds. Since the median luminosities (at  $1500 \text{ Å}$ ) of the quasars in the three samples do not positively correlate with the strength of the high-ionization absorption lines in the composite spectra, the stronger absorption from the NV, Si IV, and C IV doublets could be an indicator of the proximity to the quasars.

### 3.4.2. Comparison with Associated SLLSs and Intervening DLAs

In this section, we create stacked spectra of associated SLLSs and intervening DLAs with  $\log N(\text{H I}) = 20.30 \pm 0.20$ ,  $21.0 \pm 0.20$ , and  $21.50 \pm 0.20$ . The SLLSs are chosen from the  $S_{\text{QSO}}^3$  sample, and the intervening DLAs are from Noterdaeme et al. (2012). Our sample of SLLSs and intervening DLAs each contain 164 and 6090 (with 486 DLAs with  $\log N(\text{H I}) = 20.30 \pm 0.20$ , 1537 DLAs with  $\log N(\text{H I}) = 21.00 \pm 0.20$ , and 4067 DLAs with  $\log N(\text{H I}) = 21.50 \pm 0.20$ ) spectra, respectively. In this study, we choose only those SLLSs with  $10^{19.5} \text{ cm}^{-2} \leq N(\text{H I}) \leq 10^{20} \text{ cm}^{-2}$ . This choice is motivated by the fact that the low-ionization absorption lines in ghostly absorbers (with which the SLLSs are compared) are very strong. To create the stacked spectra, we first randomly choose 30 spectra from each sample and stack them. We repeat this process 100 times. The median of these 100 spectra is taken as the final stacked spectrum, and their standard deviation is taken as the uncertainty spectrum.

Figure 17 presents the spectral regions of some important transitions in the stacked spectra of the ghostly absorbers, SLLSs, and intervening DLAs. As shown in this figure, absorptions from high-ionization species are the strongest in ghostly absorbers. These absorption lines are all stronger in



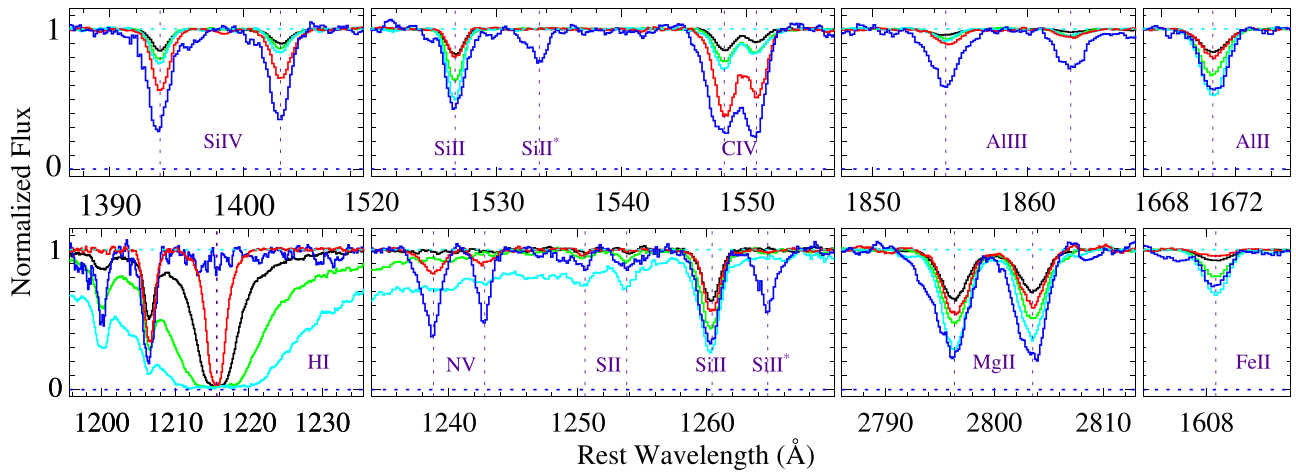


**Figure 17.** Some important transitions detected in the composite spectra of ghostly absorbers (blue curves), SLLSs (red curves), and intervening DLAs with  $\log N(\text{H I}) = 20.30$  (black curves), 21.0 (green curves), and 21.50 (cyan curves).

SLLSs compared to what is seen in intervening DLAs. The AlIII absorption, which is also the strongest in ghostly absorbers, is almost similar in SLLSs and intervening DLAs. The striking feature in Figure 17 is the presence of strong absorption from fine structure states in ghostly absorbers and the absence of such absorption in other absorbers. From this figure, one can see that the absorption properties of ghostly absorbers are uniquely different from those of the other categories of absorbers. Figures 18 and 19 show the spectra of the ghostly absorbers for which hydrogen column density is estimated.

### 3.5. Physical Properties of the Absorbers

#### 3.5.1. Constraining the Ionization Parameter and the Gas Temperature

In this section, we construct some photoionization models using the code CLOUDY (Mathews & Ferland 1987) in order to roughly estimate the gas temperature and the ionization parameter. The latter is defined as the ratio of the density of hydrogen-ionizing photons to the hydrogen density. We construct a series of CLOUDY models for a range of ionization parameters,  $U$ , varying from  $\log(U) = -3.0$  to  $+1.0$ . For each ionization parameter, the calculation is stopped when a neutral hydrogen column density of  $\log N(\text{H I}) = 21.30$  is reached. The relative abundance of elements is assumed to be solar, and the observed silicon abundance,  $[\text{Si}/\text{H}] \sim -1$ , is taken as the gas metallicity in the model cloud. The adopted spectral energy distribution comprises the standard AGN spectrum of Mathews & Ferland (1987), the Haardt–Madau metagalactic UV spectrum (Haardt & Madau 1996), and the CMB radiation of both at  $z = 2.50$ , which is the median redshift of our ghostly absorbers.

Inspection of these photoionization models shows that the N V column density of  $\log(N \text{ V}) \sim 14.15$ , measured from the composite spectrum of eclipsing DLAs with weak emission, is reproduced only when  $\log(U) \sim -1.0$ . We also checked that when  $\log(U) \lesssim -2.0$ , the predicted N V column density is  $\log(N \text{ V}) \lesssim 12.0$ , which is so small that its corresponding absorption lines would be hardly detected, if at all, in the SDSS spectra. So, it is highly likely that the ionization parameter is  $\log(U) \sim -1.0$ . This is similar to what Fathivavsari et al. (2015) found for an eclipsing DLA toward the quasar J0823+0529.

For eclipsing DLAs with strong emission and also for ghostly absorbers, we will assume the same ionization parameter ( $\log(U) \sim -1.0$ ), although the stronger absorption from high-ionization species (especially N V) and the presence of absorption from O I\*\* hint at the possibility that the ionization parameter is higher in these absorbers. Precise measurements of the ionization parameter would be possible by follow-up high-resolution spectroscopy of our eclipsing and ghostly absorbers.

Our CLOUDY models also show that the electron temperature,  $T_e$ , in the regions of the cloud where low-ionization species are dominant is  $\sim 10,000$  K. Moreover, the  $n_e/n_{\text{H}^0}$  and  $n_p/n_{\text{H}^+}$  in these regions are  $\sim 0.3$  and  $\sim 0.25$ , respectively. We will use these values to constrain the gas density (in Section 3.5.2) and the DLA–QSO distance (in Section 3.5.3).

Our CLOUDY models also show that the electron temperature,  $T_e$ , in the regions of the cloud where low-ionization species are dominant is  $\sim 10,000$  K. Moreover, the  $n_e/n_{\text{H}^0}$  and  $n_p/n_{\text{H}^+}$  in these regions are  $\sim 0.3$  and  $\sim 0.25$ , respectively. We will use these values to constrain the gas density (in Section 3.5.2) and the DLA–QSO distance (in Section 3.5.3).

#### 3.5.2. Constraining the Gas Density

In this section, we will use absorption from the Si II fine structure states to put some constraints on the gas density. Fine structure levels can be populated by collisions, radiative pumping due to a local radiation field, and direct excitation by the CMB radiation (Silva & Viegas 2002; Wolfe et al. 2003, 2008; Srianand et al. 2005). However, direct excitation by the CMB radiation is negligible for Si II because the fine structure levels in Si II are so far apart from each other. If we assume that collisional excitation by atomic hydrogen, protons, and free electrons is the dominant process in populating the Si II fine structure state, then the level population can be given by

$$\frac{N(\text{Si}_{J=1/2}^+)}{N(\text{Si}_{J=3/2}^+)} = \frac{1}{2} + \frac{2.5 \times 10^4}{n_{\text{H}^0}}. \quad (4)$$

To derive this equation, we adopt an electron temperature of  $T_e = 10,000$  K,  $n_e/n_{\text{H}^0} = 0.3$ , and  $n_p/n_{\text{H}^+} = 0.25$  (see Section 3.5.1). The observed  $N(\text{Si II}^+)/N(\text{Si II})$  ratios from the composites of ghostly absorbers and eclipsing DLAs with strong and weak emission are 0.11,  $1.3 \times 10^{-2}$ , and  $1.4 \times 10^{-3}$ , respectively. We can use Equation (4) and derive from these observed ratios the hydrogen density and the characteristic size (i.e.,  $l = N(\text{H I})/n_{\text{H I}}$ ) of our ghostly and eclipsing DLA clouds.

**Table 4.**  
DLAs Characteristics

	$N(\text{Si II}^*)/N(\text{Si II})$	$\log N(\text{H I})$ ( $\text{cm}^{-2}$ )	$L_{912}$ ( $\text{erg s}^{-1} \text{\AA}^{-1}$ )	$Q$	$n_{\text{H I}}$ ( $\text{cm}^{-3}$ )	$l$ (pc)	$r$ (pc)
Eclipsing DLAs (Weak)	$1.4 \times 10^{-3}$	21.30	$1.9 \times 10^{42}$	$3.8 \times 10^{55}$	40	16	1600
Eclipsing DLAs (Strong)	$1.3 \times 10^{-2}$	21.40	$1.4 \times 10^{42}$	$3.0 \times 10^{55}$	350	2.3	500
Ghostly Absorbers	$1.1 \times 10^{-1}$	21.00	$1.1 \times 10^{42}$	$2.3 \times 10^{55}$	3000	0.1	250

**Note.**  $N(\text{Si II}^*)/N(\text{Si II})$  ratio, neutral hydrogen column density ( $\log N(\text{H I})$ ), quasar luminosity at the Lyman limit ( $L_{912}$ ), number of hydrogen-ionizing photons ( $Q$ ), neutral hydrogen number density ( $n_{\text{H I}}$ ), characteristic size of the DLA ( $l$ ), and DLA–QSO distance ( $r$ ) for eclipsing DLAs with weak Ly $\alpha$  emission (first row), eclipsing DLAs with strong Ly $\alpha$  emission (second row), and ghostly absorbers (third row).

The results are summarized in Table 4. The detection of C I absorption seems to be consistent with the high density found for the ghostly absorbers.

As seen in Table 4, the gas is progressively getting denser, and the cloud becomes smaller in size as one goes from the eclipsing DLAs with weak emission to the ghostly absorbers. It could be possible that the gas is compressed by the interaction with outflowing gas, and that denser clouds are located closer to the AGN where outflows are stronger (see next section).

### 3.5.3. Constraining the DLA–QSO Distance

By knowing the ionization parameter,  $U$ , and the gas density,  $n_{\text{H I}}$ , one can estimate the DLA–QSO distance using the following relation:

$$r = \sqrt{\frac{Q}{4 \pi U n_{\text{H I}} c}}, \quad (5)$$

where  $Q$  is the number of hydrogen-ionizing photons, and  $c$  is the speed of light. To determine  $Q$ , we first estimate the flux (and then the quasar luminosity,  $L_{912}$ ) at the Lyman limit by extrapolating, with a power law, the continuum observed at 6100 and 8100 Å. We then assume a flat spectrum (i.e.,  $L_\nu = L_{912}$ ) and integrate  $L_\nu/h\nu$  over the energy range 1 to 20 Ryd (Fathivavsari et al. 2015) to estimate the number of hydrogen-ionizing photons. When  $Q$  is known, one can use Equation (5) to get the DLA–QSO distance. The results are summarized in Table 4. As shown in this table, these distances, albeit being rough estimates, are consistent with our proposed scenario in which ghostly absorbers are located closer to the quasars compared to eclipsing DLAs.

## 4. Summary and Conclusion

In this paper, we have presented and studied a sample of 30 ghostly absorbers from SDSS-III BOSS DR12. We compared the properties of the ghostly absorbers with those of the eclipsing DLAs from Paper I. By analyzing the spectra of these DLAs, we found an interesting sequence in the observed properties of ghostly and eclipsing DLAs. The sequence is such that the eclipsing DLAs with strong emission always exhibit properties that are intermediate between what is seen in the ghostly and eclipsing DLAs with weak emission. Below, we summarize these observed sequences:

- (i) We found that the  $b$ -values obtained from the single-component curve of growth for the Lyman series absorption lines progressively get larger from the eclipsing DLAs with weak emission to ghostly absorbers.

If we attribute the  $b$ -values to the turbulence, then higher  $b$ -values would imply that the absorber is experiencing stronger turbulence, and that the cloud may be located closer to the quasar.

- (ii) The strength of the absorption from the excited states of Si II and C II also exhibits a sequence in which ghostly absorbers show the strongest absorption in these transitions. Since fine structure states can be populated by collisional and radiative excitation, stronger absorption from these transitions would imply higher gas density or proximity to the quasar. Higher resolution spectra of these DLAs are required in order to break the degeneracy between the gas density and proximity to the quasar.
- (iii) The absorption from high-ionization species (e.g., Si IV, C IV, and N V) is the strongest in the ghostly absorbers and the weakest in the eclipsing DLAs with weak emission. Stronger N V absorption could be due to higher metallicity or a higher level of ionization in the cloud. Since ghostly and eclipsing DLAs seem to have almost similar metallicities (i.e.,  $\log Z/Z_\odot \sim -1.0$ ), stronger N V absorption could be attributed to higher ionization, and maybe to the proximity to the quasar.
- (iv) We employed three different approaches to estimate the reddening of the background quasar by the dust in the ghostly and eclipsing DLAs. We found that the dust extinction is highest in ghostly absorbers. Using the template-matching technique, we found  $A_V = 0.19 \pm 0.06$ ,  $0.11 \pm 0.07$ , and  $0.05 \pm 0.05$  for ghostly and eclipsing DLAs with strong and weak emission, respectively.

Taken together, these results are suggestive that the ghostly absorbers are located closer to the quasars and are perhaps of higher densities compared to the eclipsing DLAs. In Paper I, we argued that the eclipsing DLAs with strong Ly $\alpha$  emission are denser and closer to the quasars, compared to eclipsing DLAs with weak emission. We proposed that eclipsing DLAs could be the product of the collision between infalling and outflowing gas, and that when the Ly $\alpha$  emission in the DLA trough is stronger, the collision occurs closer to the quasars. This scenario is corroborated by the correlation found between the strength of the Ly $\alpha$  emission detected in the DLA trough and the strength of the absorption from the fine structure states (indicative of the gas density or proximity to the quasar) and high-ionization species (indicative of the ionization level).

We now extend this scenario and propose that ghostly absorbers are from the same population as eclipsing DLAs, except that they are so dense that the projected size of the DLA is much smaller than that of the BLR. In this case, the leaked

emission from the BLR would fill the DLA absorption trough, and consequently no apparent DLA absorption would be detected in the spectrum. We recall that in eclipsing DLAs (especially those with  $\text{Ly}\alpha$  emission in their troughs) the gas density is low (high) enough that the projected size of the DLA cloud is larger (smaller) than that of the BLR (NLR or star-forming regions in the host galaxy). That is why, in the spectra of eclipsing DLAs (with or without  $\text{Ly}\alpha$  emission), the DLA absorption profile is clearly visible.

If eclipsing and ghostly absorbers are the product of the interaction between infalling and outflowing gas, then higher densities in ghostly absorbers would imply that the interaction should have occurred closer to the quasars. Since regions close to quasars are expected to be highly turbulent, the larger widths of the hydrogen absorption lines in ghostly absorbers seem to be consistent with the picture in which ghostly absorbers (compared to eclipsing DLAs) probe regions closer to the quasars. The higher level of ionization along with the higher  $N(\text{Si II}^*)/N(\text{Si II})$  ratio in ghostly absorbers is also consistent with this scenario.

Higher resolution spectra of some of our best eclipsing and ghostly absorber systems would allow detailed analysis of the kinematics and ionization state of the gas, which would in turn help confirm the validity of the scenario presented here and in Paper I.

H.F. would like to thank the referee for useful comments and the Iranian National Observatory for their support during this project. H.F. also acknowledges conversations with Narges Jamialahmadi, Habib Khosroshahi, Hadi Rahmani, Ragunathan

Srianand, Pasquier Noterdaeme, and Patrick Petitjean during the preparation of this manuscript. Funding for SDSS-III has been provided by the Alfred P. Sloan Foundation, the Participating Institutions, the National Science Foundation, and the U.S. Department of Energy Office of Science. The SDSS-III website is <http://www.sdss3.org/>.

SDSS-III is managed by the Astrophysical Research Consortium for the Participating Institutions of the SDSS-III Collaboration including the University of Arizona, the Brazilian Participation Group, Brookhaven National Laboratory, Carnegie Mellon University, University of Florida, the French Participation Group, the German Participation Group, Harvard University, the Instituto de Astrofísica de Canarias, the Michigan State/Notre Dame/JINA Participation Group, Johns Hopkins University, Lawrence Berkeley National Laboratory, Max Planck Institute for Astrophysics, Max Planck Institute for Extraterrestrial Physics, New Mexico State University, New York University, Ohio State University, Pennsylvania State University, University of Portsmouth, Princeton University, the Spanish Participation Group, University of Tokyo, University of Utah, Vanderbilt University, University of Virginia, University of Washington, and Yale University.

## Appendix A Some Additional Figures

The Voigt profile fit to the Lyman series absorption lines (Figure 18) and the reconstruction of the quasar spectrum in the Lyman- $\alpha$  spectral region (Figure 19).

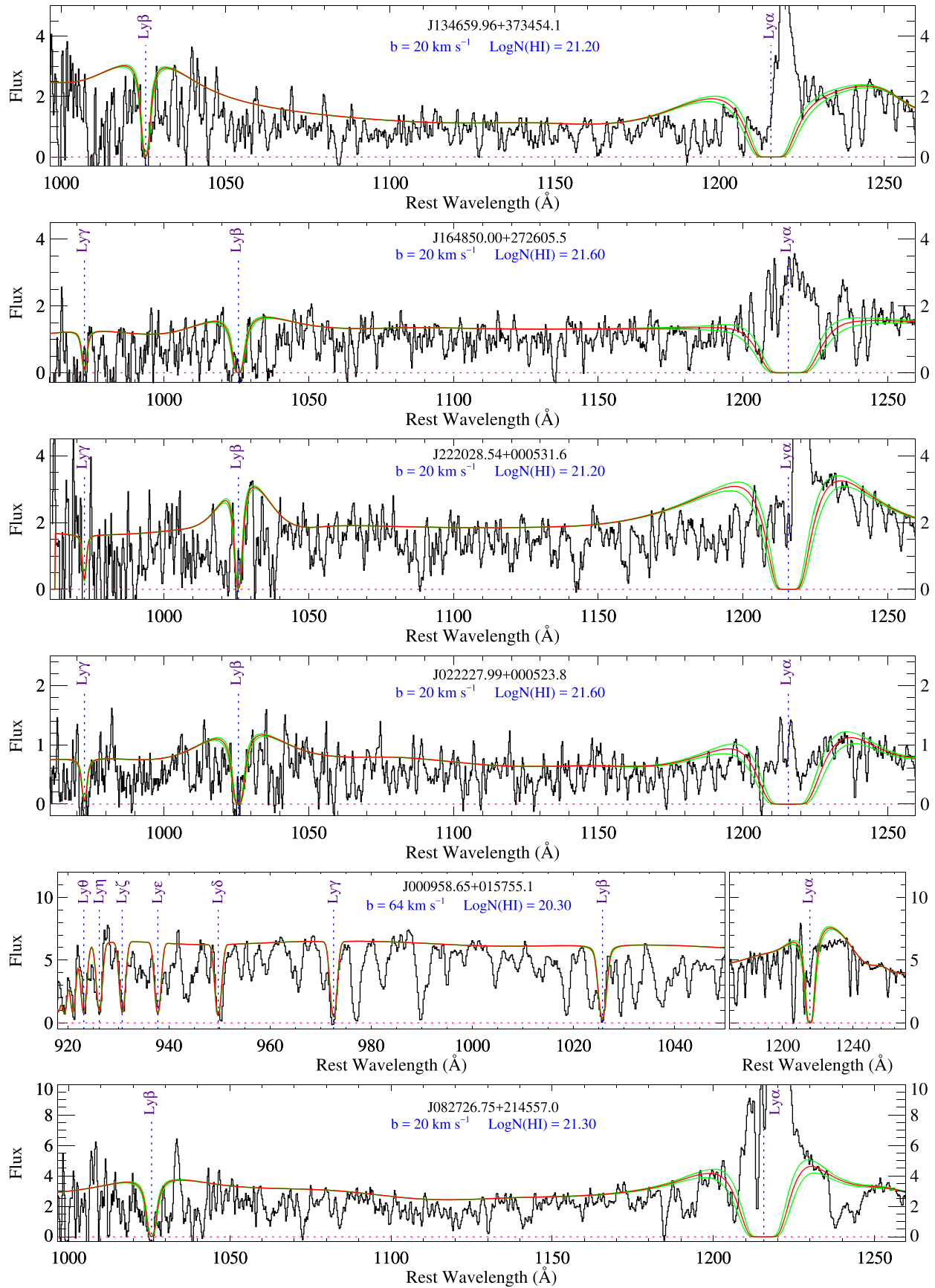


Figure 18. Same as Figure 2.



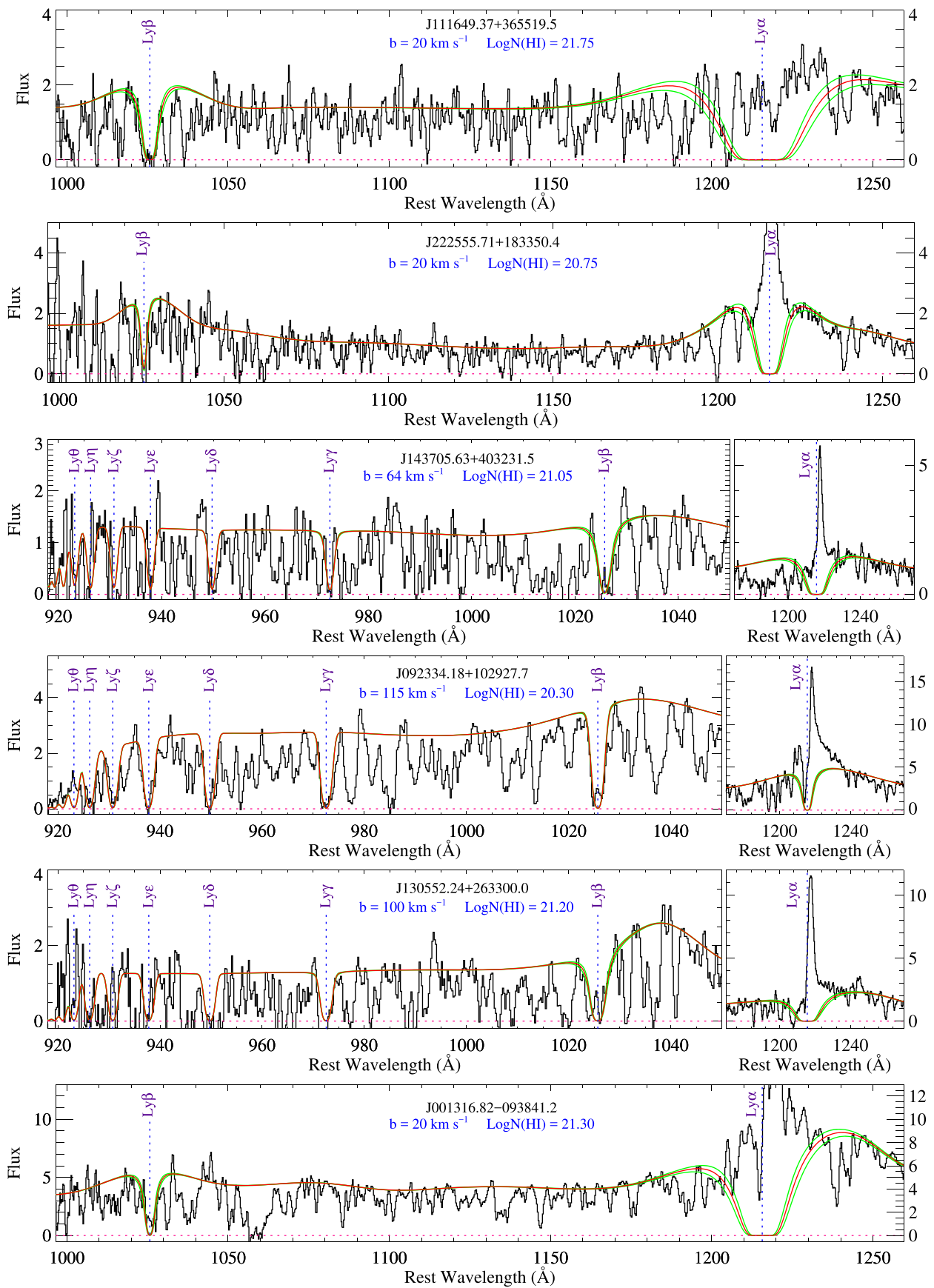


Figure 18. (Continued.)

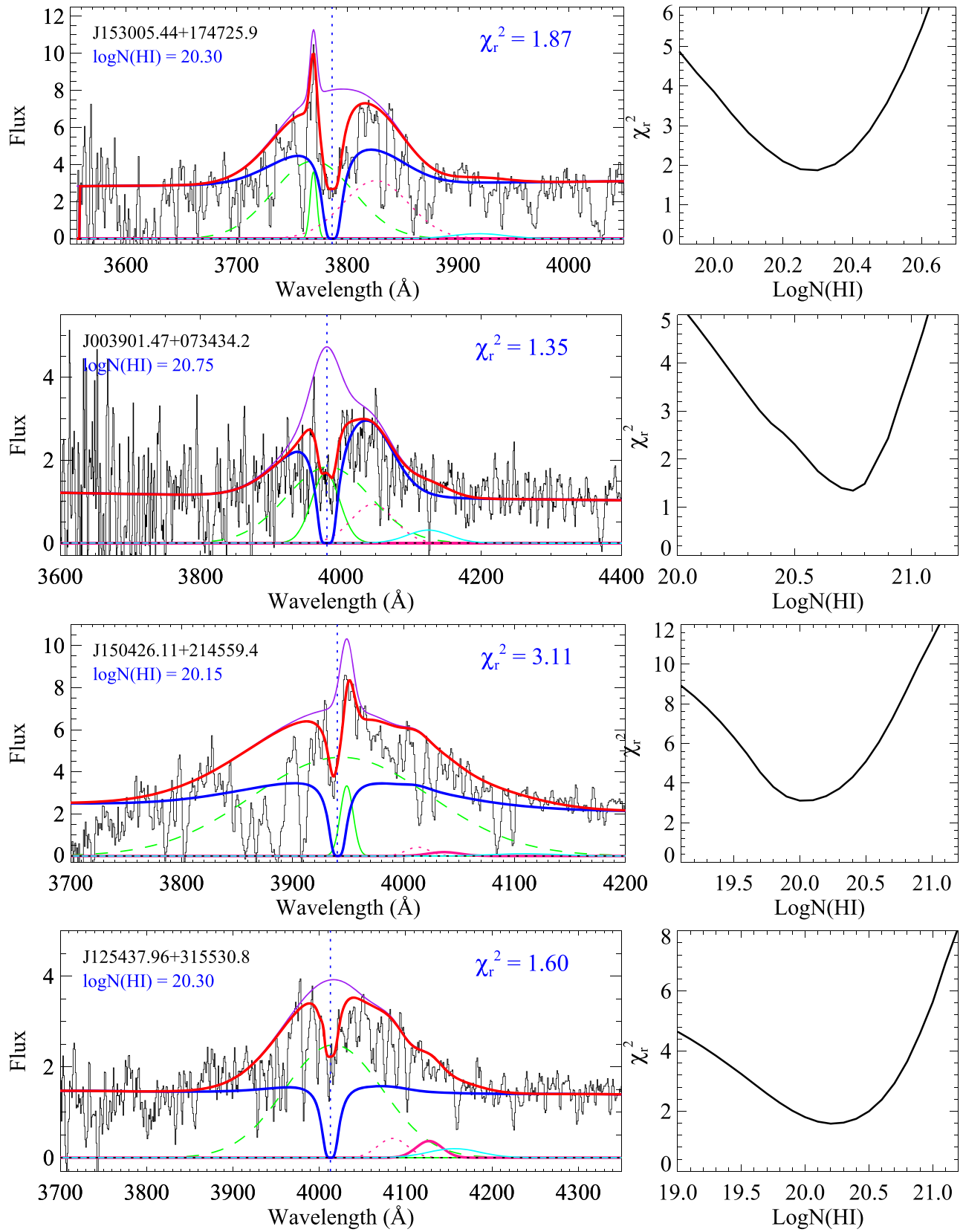


Figure 19. Same as Figure 5.

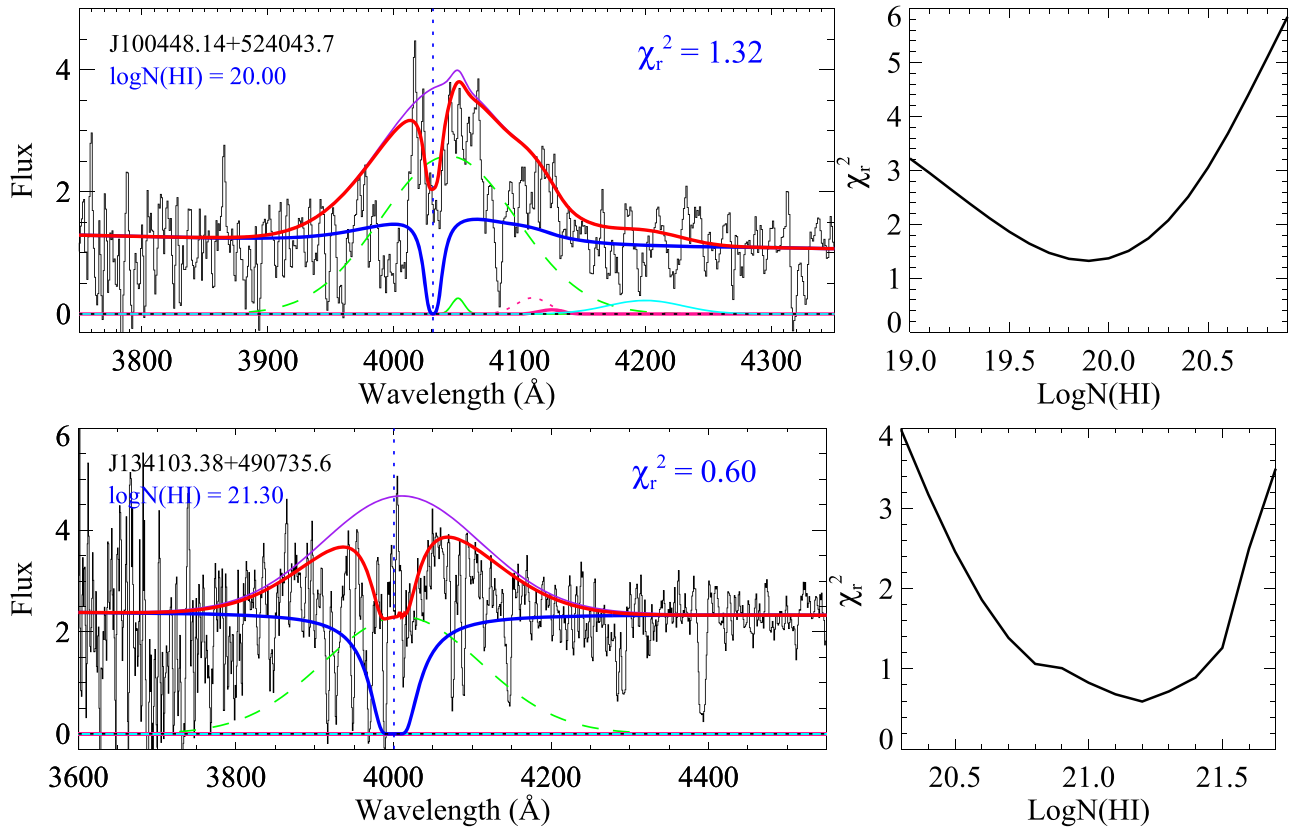


Figure 19. (Continued.)

## References

- Audibert, A., Combes, F., García-Burillo, S., & Salomé, P. 2017, *FrASS*, **4**, 58
- Berg, T. A. M., Ellison, S. L., Prochaska, J. X., et al. 2017, *MNRAS*, **464**, L56
- Chisholm, J., Tremonti, C. A., Leitherer, C., et al. 2015, *ApJ*, **811**, 149
- Cresci, G., Mannucci, F., Maiolino, R., et al. 2010, *Natur*, **467**, 811
- Dawson, K. S., Schlegel, D. J., Ahn, C. P., et al. 2013, *AJ*, **145**, 10
- Di Matteo, P., Montuori, M., Lehnert, M. D., Combes, F., & Semelin, B. 2011, in *IAU Symp. 277, Tracing the Ancestry of Galaxies*, ed. C. Carignan, F. Combes, & K. C. Freeman (Cambridge: Cambridge Univ. Press), 246
- Dutta, R., Srianand, R., & Gupta, N. 2018, *MNRAS*, **480**, 947
- Ellison, S. L., Murphy, M. T., & Dessauges-Zavadsky, M. 2009, *MNRAS*, **392**, 998
- Ellison, S. L., Prochaska, J. X., Hennawi, J., et al. 2010, *MNRAS*, **406**, 1435
- Fathivavsari, H., Ajabshirizadeh, A., & Koutchmy, S. 2014, *Ap&SS*, **353**, 347
- Fathivavsari, H., Petitjean, P., Jamialahmadi, N., et al. 2018, *MNRAS*, **477**, 5625
- Fathivavsari, H., Petitjean, P., Ledoux, C., et al. 2013, *MNRAS*, **435**, 1727
- Fathivavsari, H., Petitjean, P., Noterdaeme, P., et al. 2015, *MNRAS*, **454**, 876
- Fathivavsari, H., Petitjean, P., Noterdaeme, P., et al. 2016, *MNRAS*, **461**, 1816
- Fathivavsari, H., Petitjean, P., Zou, S., et al. 2017, *MNRAS*, **466**, L58
- Faucher-Giguère, C.-A., & Kereš, D. 2011, *MNRAS*, **412**, L118
- Finley, H., Bouché, N., Contini, T., et al. 2017, *A&A*, **605**, A118
- Finley, H., Petitjean, P., Pâris, I., et al. 2013, *A&A*, **558**, A111
- Fitzpatrick, E. L., & Massa, D. 2007, *ApJ*, **663**, 320
- Fox, A. J., Prochaska, J. X., Ledoux, C., et al. 2009, *A&A*, **503**, 731
- Fumagalli, M., Prochaska, J. X., Kasen, D., et al. 2011, *MNRAS*, **418**, 1796
- Fynbo, J. P. U., Krogager, J.-K., Venemans, B., et al. 2013, *ApJS*, **204**, 6
- Giavalisco, M., Vanzella, E., Salimbeni, S., et al. 2011, *ApJ*, **743**, 95
- Goerdt, T., Dekel, A., Sternberg, A., et al. 2010, *MNRAS*, **407**, 613
- Gordon, K. D., Clayton, G. C., Misselt, K. A., Landolt, A. U., & Wolff, M. J. 2003, *ApJ*, **594**, 279
- Haardt, F., & Madau, P. 1996, *ApJ*, **461**, 20
- Hennawi, J. F., Prochaska, J. X., Kollmeier, J., & Zheng, Z. 2009, *ApJL*, **693**, L49
- Herbert-Fort, S., Prochaska, J. X., Dessauges-Zavadsky, M., et al. 2006, *PASP*, **118**, 1077
- Hewett, P. C., & Wild, V. 2010, *MNRAS*, **405**, 2302
- Jenkins, E. B. 1986, *ApJ*, **304**, 739
- Kaplan, K. F., Prochaska, J. X., Herbert-Fort, S., Ellison, S. L., & Dessauges-Zavadsky, M. 2010, *PASP*, **122**, 619
- Kereš, D., Katz, N., Weinberg, D. H., & Davé, R. 2005, *MNRAS*, **363**, 2
- Khare, P., Kulkarni, V. P., Lauroesch, J. T., et al. 2004, *ApJ*, **616**, 86
- Kimm, T., Slyz, A., Devriendt, J., & Pichon, C. 2011, *MNRAS*, **413**, L51
- Krawczyk, C. M., Richards, G. T., Gallagher, S. C., et al. 2015, *AJ*, **149**, 203
- Lehner, N., Howk, J. C., Thom, C., et al. 2012, *MNRAS*, **424**, 2896
- Martin, D. C., Matuszewski, M., Morrissey, P., et al. 2016, *ApJL*, **824**, L5
- Martin, P. G. 1988, *ApJS*, **66**, 125
- Mathews, W. G., & Ferland, G. J. 1987, *ApJ*, **323**, 456
- Murphy, M. T., & Liske, J. 2004, *MNRAS*, **354**, L31
- Namekata, D., Umemura, M., & Hasegawa, K. 2014, *MNRAS*, **443**, 2018
- Nestor, D. B., Turnshek, D. A., & Rao, S. M. 2006, *ApJ*, **643**, 75
- Noterdaeme, P., Ledoux, C., Zou, S., et al. 2018, *A&A*, **612**, A58
- Noterdaeme, P., Petitjean, P., Carithers, W. C., et al. 2012, *A&A*, **547**, L1
- Pâris, I., Petitjean, P., Ross, N. P., et al. 2017, *A&A*, **597**, A79
- Perrotta, S., D'Odorico, V., Prochaska, J. X., et al. 2016, *MNRAS*, **462**, 3285
- Prevot, M. L., Lequeux, J., Maurice, E., Prevot, L., & Rocca-Volmerange, B. 1984, *A&A*, **132**, 389
- Prochaska, J. X. 2006, *ApJ*, **650**, 272
- Prochaska, J. X., & Herbert-Fort, S. 2004, *PASP*, **116**, 622
- Rahmani, H., Péroux, C., Augustin, R., et al. 2018a, *MNRAS*, **474**, 254
- Rahmani, H., Péroux, C., Schroetter, I., et al. 2018b, *MNRAS*, **480**, 5046
- Rahmani, H., Srianand, R., Noterdaeme, P., & Petitjean, P. 2010, *MNRAS*, **409**, L59
- Ranjan, A., Noterdaeme, P., Krogager, J.-K., et al. 2018, *A&A*, **618**, A184
- Rao, S. M., Turnshek, D. A., & Briggs, F. H. 1995, *ApJ*, **449**, 488
- Rao, S. M., Turnshek, D. A., & Nestor, D. B. 2006, *ApJ*, **636**, 610
- Rauch, M., Haehnelt, M., Bunker, A., et al. 2008, *ApJ*, **681**, 856
- Rubin, K. H. R., Prochaska, J. X., Koo, D. C., & Phillips, A. C. 2012, *ApJL*, **747**, L26
- Rupke, D. S. N., Kewley, L. J., & Barnes, J. E. 2010, *ApJL*, **710**, L156
- Schroetter, I., Bouché, N., Wendt, M., et al. 2016, *ApJ*, **833**, 39
- Selsing, J., Fynbo, J. P. U., Christensen, L., & Krogager, J.-K. 2016, *A&A*, **585**, A87
- Sillero, E., Tissera, P. B., Lambas, D. G., & Michel-Dansac, L. 2017, *MNRAS*, **472**, 4404

- Silva, A. I., & Viegas, S. M. 2002, [MNRAS](#), **329**, 135
- Srianand, R., Petitjean, P., Ledoux, C., Ferland, G., & Shaw, G. 2005, [MNRAS](#), **362**, 549
- Srianand, R., Petitjean, P., Ledoux, C., & Hazard, C. 2002, [MNRAS](#), **336**, 753
- Steidel, C. C., Erb, D. K., Shapley, A. E., et al. 2010, [ApJ](#), **717**, 289
- Stewart, K. R., Kaufmann, T., Bullock, J. S., et al. 2011a, [ApJL](#), **735**, L1
- Stewart, K. R., Kaufmann, T., Bullock, J. S., et al. 2011b, [ApJ](#), **738**, 39
- Sur, S., Scannapieco, E., & Ostriker, E. C. 2016, [ApJ](#), **818**, 28
- Torrey, P., Cox, T. J., Kewley, L., & Hernquist, L. 2012, [ApJ](#), **746**, 108
- van de Voort, F., Schaye, J., Altay, G., & Theuns, T. 2012, [MNRAS](#), **421**, 2809
- Weymann, R. J., Morris, S. L., Foltz, C. B., & Hewett, P. C. 1991, [ApJ](#), **373**, 23
- Wild, V., & Hewett, P. C. 2005, [MNRAS](#), **361**, L30
- Wild, V., Hewett, P. C., & Pettini, M. 2006, [MNRAS](#), **367**, 211
- Wolfe, A. M., Prochaska, J. X., & Gawiser, E. 2003, [ApJ](#), **593**, 215
- Wolfe, A. M., Prochaska, J. X., Jorgenson, R. A., & Rafelski, M. 2008, [ApJ](#), **681**, 881
- Wood, C. M., Tremonti, C. A., Calzetti, D., et al. 2015, [MNRAS](#), **452**, 2712
- Xie, X., Zhou, H., Pan, X., et al. 2018, [ApJ](#), **858**, 32
- York, D. G., Khare, P., Vanden Berk, D., et al. 2006, [MNRAS](#), **367**, 945